RESEARCH ARTICLE SUMMARY

DEVELOPMENT

Oxytocin signaling regulates maternally directed behavior during early life

Daniel D. Zelmanoff, Rebecca Bornstein, Menachem Kaufman, Julien Dine, Jonas Wietek, Anna Litvin, Shaked Abraham, Savanna Cohen, Ayelet Atzmon, Ido Porat, Ofer Yizhar*

Full article and list of author affiliations: https://doi.org/10.1126/science.ado5609

INTRODUCTION: Oxytocin is a brain hormone that plays a critical role in regulating social behavior. Although much research has focused on how oxytocin supports adult behaviors such as pair-bonding and caregiving, far less is known about how this system functions during early life. The early postnatal period is a time of critical social interactions between infants and caregivers, and disruptions during this period may contribute to developmental disorders. Notably, expression of the oxytocin receptor peaks during infancy in both humans and mice, suggesting that this period represents a critical window of heightened sensitivity to oxytocin signaling. However, technical challenges have limited the study of the oxytocin system during this sensitive time of brain development. As a result, the role of oxytocin in shaping social behavior during infancy remains poorly understood.

RATIONALE: We set out to investigate how oxytocin influences pup behavior during a brief separation from the mother and littermates and subsequent reunion. We focused on vocal communication, as rodent pups emit ultrasonic vocalizations that signal distress but may also reflect social motivation and need. We combined detailed behavioral analysis with fiber photometry, pharmacological intervention, and a novel optogenetic strategy built on wireless silencing of oxytocin neurons in freely behaving pups—a technical advance that overcomes prior limitations in studying brain circuits during early life.

RESULTS: Pups that were acutely separated from their mother and littermates displayed a substantial increase in vocalizations upon reunion, especially when in close proximity to their mother. The rate and type of vocalizations were modulated by nipple attachment behavior. We found that hypothalamic oxytocin neurons increased their activity upon separation, and that this activity was tightly linked with the emission of vocalizations. Blocking the oxytocin receptor in pups during separation reduced nipple attachment and altered the pattern of vocal behavior both during separation and reunion. For increased temporal precision, we developed a new optogenetic method using a highly light-sensitive, red-shifted inhibitory opsin (eOPN3). This allowed us to wirelessly silence oxytocin neurons in untethered pups. We found that silencing oxytocin neurons during separation disrupted vocal—but not nonvocal—behavior during both the separation and reunion.

CONCLUSION: Our findings reveal a specific role for oxytocin in shaping maternally directed behavior during infancy. We also introduce a noninvasive optogenetic approach for studying brain circuits in developing animals, opening new opportunities to investigate the neural mechanisms underlying early life social behavior. Our work emphasizes the need to gain a more nuanced understanding of oxytocin function and provides a technical platform for studying the social brain during its most formative stages. □

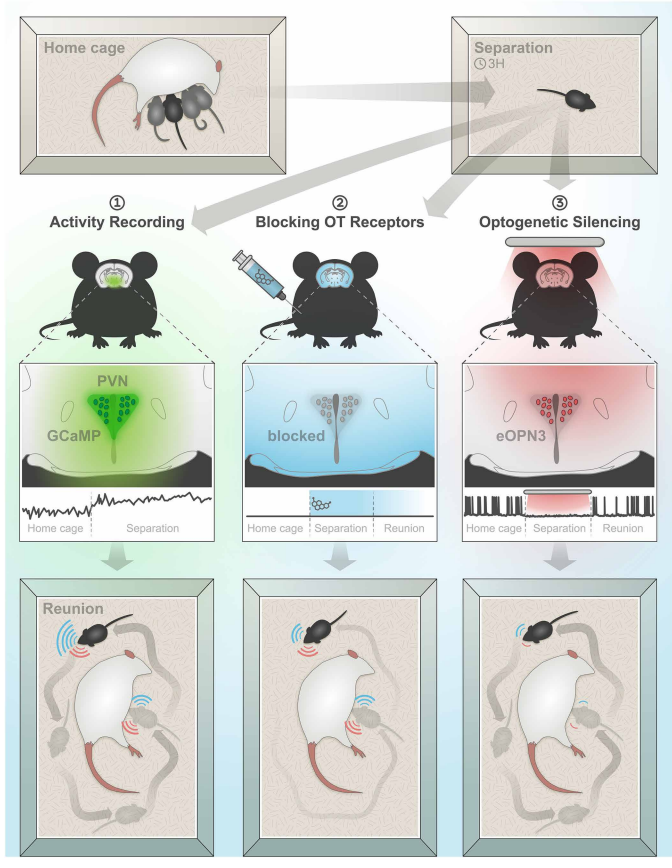

Oxytocin shapes infant behavior toward the mother. To explore the role of oxytocin in early life, we separated pups from their mother (top) and then reunited them while tracking vocal and nonvocal behaviors (bottom). Oxytocin cells in the pups' brain increased their activity upon separation (1), while blocking the oxytocin receptor (2) or optogenetic silencing of oxytocin neurons (3) altered the pattern of maternally directed behavior upon reunion, highlighting an important role for oxytocin during early life.

*Corresponding author. Email: ofer.yizhar@weizmann.ac.il. Cite this article as Daniel D. Zelmanoff *et al.*, *Science* **389**, eado5609 (2025). DOI: 10.1126/science.ado5609

DEVELOPMENT

Oxytocin signaling regulates maternally directed behavior during early life

Daniel D. Zelmanoff[1,2], Rebecca Bornstein[1,2], Menachem Kaufman[1,2], Julien Dine[1,2]†, Jonas Wietek[1,2]‡, Anna Litvin[1,2], Shaked Abraham[1,2], Savanna Cohen[1,2], Ayelet Atzmon[1,2], Ido Porat[1,2], Ofer Yizhar[1,2]*

Oxytocin is essential in shaping social behavior across the lifespan. Although the role of oxytocin signaling in parental care has been widely investigated, little is known about its function in social behavior during early life. We studied the role of oxytocin in mouse pup social behavior during acute separation from the mother as well as upon reunion. The activity of oxytocin neurons was increased by acute maternal separation. Behaviorally, maternally separated pups emitted more ultrasonic vocalizations upon reunion, which were further modulated by nipple attachment behavior. These effects were attenuated by blocking the oxytocin receptor during maternal separation. Optogenetic silencing of oxytocin neurons during maternal separation disrupted vocal behavior during separation and reunion. Our findings reveal an important role of oxytocin in context-dependent vocal communication in mouse pups.

Oxytocin (OT), a nonapeptide secreted from the paraventricular (PVN) and supraoptic (SON) nuclei in the hypothalamus of the mammalian brain, is widely recognized as a key neuromodulator involved in a wide array of social behaviors [reviewed in (*1*)]. Over the last 50 years, numerous animal studies have pointed to a central role for OT in many aspects of social behaviors, including pair bonding (*2*), social learning (*3*–*5*), parental care (*6*–*8*), and adult-infant attachment (*9*, *10*). Furthermore, animal models with disrupted OT signaling display behavioral impairments in social function, reminiscent of core symptoms in neurodevelopmental disorders such as autism spectrum disorder (ASD) (*5*, *11*–*13*, *14*–*16*). Although OT treatment is suggested as a potential treatment to social deficits in ASD patients (*17*–*19*), such clinical studies have culminated in mixed results (*20*–*22*). This suggests that our basic understanding of the OT system and its role in social behavior is incomplete. In particular, very little is known about the role of OT in regulating ongoing behavioral adaptations during early life, in part due to a paucity of tools available to study the neonatal brain during this sensitive period of development. In the current study, we set out to explore the role of the OT system in mouse pups, in the context of acute separation from and reunion with the mother.

Acute maternal separation increases maternally directed behavior upon reunion

In the mouse pup brain, the neural mechanisms engaged during short-term transitions from social deprivation to engagement during early life are not well understood. To study this, we used a modified maternal separation paradigm to characterize reunion-related ultrasonic vocalizations (USVs) and affiliative behaviors of 15-day-old (P15) mice following 3 hours of maternal separation, and provide a framework for examining the effects of OT manipulations on these behaviors.

We first investigated how separation influences pup behavior during reunion, allowing for freely behaving dam-pup interactions during the reunion phase (Fig. 1A and movie S1). In this assay, reunited pups rapidly engaged in social interaction with the dam that persisted throughout the 10-min reunion phase. Although locomotion did not differ between separated and unseparated dam-pup dyads (fig. S1A), separated pups spent considerably more time in close proximity to their dams over the course of the reunion (Fig. 1B). Additionally, the mean dam-pup distance was smaller for separated than for unseparated pups [MS: 11.453 ± 0.572 cm; 13.369 ± 0.325 cm; $t_{(29)} = 2.861$, $P = 0.008$], suggesting that maternal separation enhances maternally directed movement upon reunion.

We next analyzed the dynamics of USV emission over time. We found that previously separated mother-pup (MP) dyads vocalized more frequently at the beginning of the trial compared with unseparated animals (fig. S1B) coinciding with close dyad proximity (Fig. 1C). However, USV rates among separated animals declined more rapidly. After approximately the first minute of the reunion, we detected a change point in USV rates of separated and unseparated animals, indicating a substantial shift in vocal behavior at this time (fig. S1B). These results suggest that in freely behaving MP dyads, the effects of maternal separation on vocal behavior are most prominent early in the reunion.

Using k-means clustering of USV spectral properties, we identified three distinct USV clusters. Maternally separated dyads emitted a higher rate of narrow-bandwidth, high-frequency (>70 kHz) calls (Fig. 1D), which were most prominent early in the reunion (fig. S1C). These findings indicate that maternal separation modulates both vocal and nonvocal pup behaviors.

Although these findings showed that acute maternal separation increases MP interactions upon reunion, we could not isolate pup USVs or rule out the participation of the dam as the driving force of social interaction. We thus designed a more controlled version of our assay in which we examined pup behavior toward an anesthetized dam (*23*, *24*). This MP assay allowed us to identify the source of USVs and focus our investigation on the pups' social behavior during the reunion.

Nipple attachment is an important MP interaction that initiates feeding interactions and is thus crucial for survival (*25*, *26*). In the reunion phase of the MP assay, pups were allowed to freely explore the testing cage and engage in nipple attachment behavior (Fig. 1, E and F). We found no differences in nipple attachment behavior in separated pups compared with unseparated control pups (Fig. 1, G and H, and fig. S2, A to C), likely due to the relatively short duration of milk deprivation in our assay (*27*, *28*).

By contrast, we found that separated pups showed robust USV emission upon reunion, primarily while in close proximity with the mother, compared with unseparated pups that displayed few USVs (Fig. 1, E, and F). This pattern of USV emission persisted in separated pups throughout the reunion (Fig. 1I), particularly when approaching the dam before the first nipple attachment (fig. S2, D to G), but also while engaging in nipple attachment (Fig. 1F). The occurrence of USV emission across varying behavioral states, both during and outside of nipple-attachment events, suggests a state-dependent use of these vocalizations (*29*).

We therefore examined whether these distinct behavioral states might be associated with distinct types of USVs. We studied the USV emission patterns recorded from separated pups during the reunion phase (fig. S2, H to K, and fig. S3). We identified three USV types: (i) USVs with narrow bandwidth and high mean frequency ("Narrow-High"); (ii) USVs with varied bandwidth and medium mean frequency ("Complex"); and (iii) USVs with narrow bandwidth and low mean frequency ("Narrow-Low"; Fig. 1J). Comparing these results with a commonly used approach that assigns USVs to predefined vocal categories (*30*, *31*) revealed a considerable overlap of some vocal categories, mainly in the Narrow-High and Narrow-Low USVs. There were, however, substantial differences in the distribution of categories across the three

[1]Department of Brain Sciences, Weizmann Institute of Science, Rehovot, Israel. [2]Department of Molecular Neuroscience, Weizmann Institute of Science, Rehovot, Israel. ***Corresponding author. Email: ofer.yizhar@weizmann.ac.il** †Present address: Boehringer Ingelheim Pharma GmbH & Co. KG, CNS Diseases, Biberach an der Riss, Germany. ‡Present address: Charité-Universitätsmedizin Berlin, corporate member of Freie Universität Berlin, and Humboldt-Universität zu Berlin, Neuroscience Research Center, Berlin, Germany.

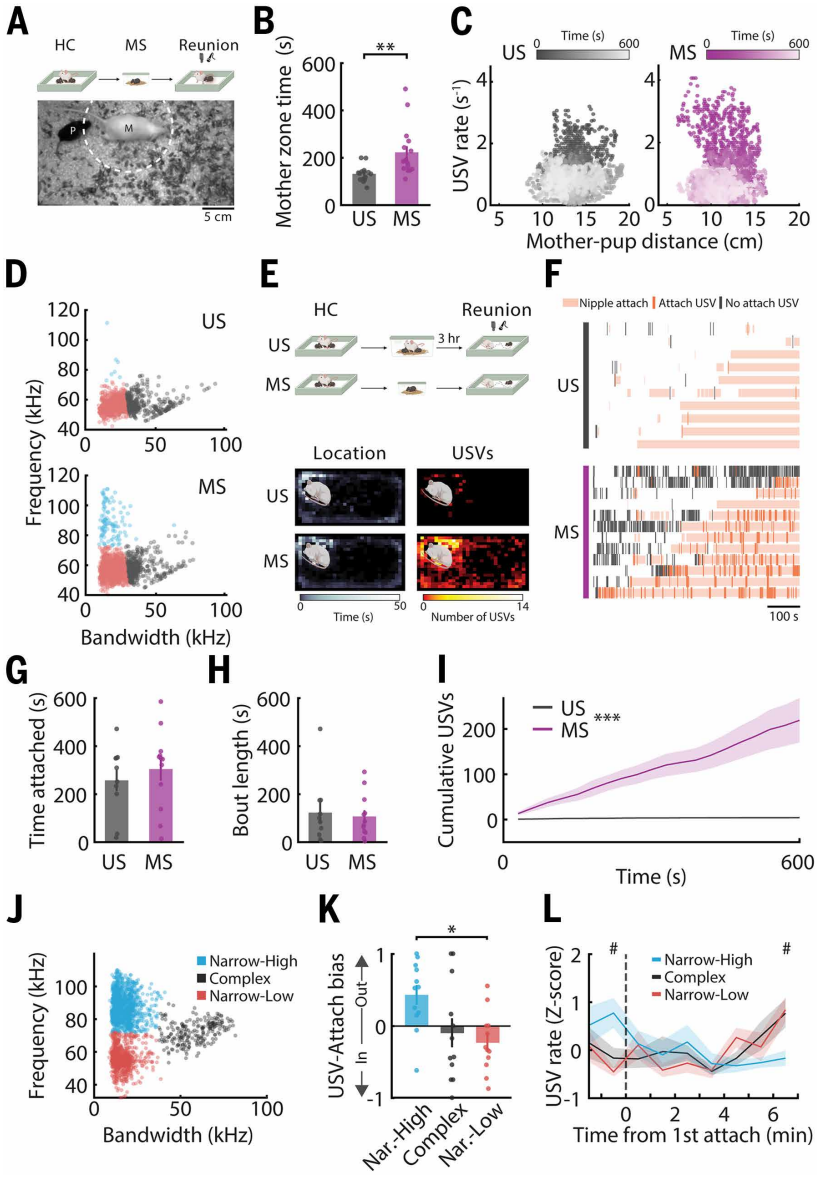

Fig. 1. Acute maternal separation increases maternally directed behavior upon reunion. (**A**) (Top) Schematic of the acute maternal separation (MS) assay. (Bottom) A representative video still from the reunion phase of the assay, showing pup (P), mother (M), and "mother zone" (dashed circle). (**B**) Total time pup spent in the "mother zone" over the 10-minute reunion for maternally separated (MS, magenta; $n = 16$) and unseparated (US, gray; $n = 15$) pups. Student's t-test $t_{(29)} = -3.208, P = 0.003$. (**C**) USV rate plotted as a function of MP distance and time, by condition. The color gradient indicates the progression of time from start (t = 0 s, dark hues) to end of the reunion (t = 600 s, light hues). (**D**) Individual USVs emitted by US (top) and MS (bottom) MP dyads within the first minute of reunion. USVs are grouped into three clusters based on bandwidth and mean frequency. (**E**) (Top) Schematics of the MP assay with an anesthetized dam illustrating unseparated (US; $n = 10$) and MS ($n = 12$) pups. (Bottom) Heat maps of the location and USV counts, averaged over 1 mm^2 bins, in relation to the dam's position in the reunion cage. (**F**) Raster plot of USVs emitted upon the reunion with the dam, showing USVs emitted within (orange ticks) and outside (gray) events of nipple attachments and overlaid with bouts of nipple attachment for each pup (shaded orange). Individual mice are sorted based on total duration of nipple attachment (ascending). (**G**) Total time of nipple attachment during reunion with the dam for MS (magenta) and US (gray) pups. Student's t-test $t_{(20)} = -0.699, P = 0.493$. (**H**) Averaged bout length of nipple attachment during reunion. Student's t-test $t_{(20)} = 0.331, P = 0.744$. (**I**) Cumulative number of USVs emitted during the reunion over 30-sec bins. Mixed-design repeated-measures (RM) ANOVA. $F_{groups(1,20)} = 20.814, P = 1.9 \times 10^{-4}$; $F_{time(1.216,24.327)} = 11.375, P = 0.002; F_{groups \times time(1.216,24.327)} = 10.727$, $P = 0.002$. (**J**) Individual USVs emitted by MS pups grouped into three clusters based on their bandwidth and mean frequency. Colors in subsequent panels correspond with this cluster analysis. (**K**) The USV-attachment bias for the three USV clusters of MS pups. Higher index values indicate greater USV emission outside nipple attachment for the specified cluster. Generalized linear mixed model (GLMM) fitting with Bonferroni-corrected post-hoc comparisons. (**L**) Normalized cluster-specific frequency of USV emission, aligned to first nipple attachment for MS pups. Linear mixed effect (LME) model to test the effect of cluster and time from first nipple attachment on USV emission with FDR-corrected post hoc comparisons (# indicates significant comparisons). Data are presented as mean ± SEM (error bars or shaded areas), $*P < 0.05$ $***P < 0.01$ $**P < 0.001$. For detailed statistical information, see tables S1 and S2.

USV types (fig. S2, L to N), suggesting that each represents a specific set of USV subtypes within the pup's vocal repertoire.

We next asked whether these USV profiles are differentially linked to distinct nipple attachment states. We found that separated pups emitted more Narrow-High USVs outside of attachment events whereas Narrow-Low USVs were more common during attachment events (Fig. 1K). Specifically, Narrow-High USVs were more prevalent before the first attachment event and gradually declined (Fig. 1L) whereas Narrow-Low and Complex USVs were less common before the first attachment event. These results, along with the overall lower number of Complex USVs in similar analyses (table S1), suggest that Narrow-High and Narrow-Low USVs are closely associated with nonattachment and attachment states, respectively. We therefore focused our subsequent analyses on these two USV types.

OT neuron activity is increased by maternal separation

We next set out to explore the role of the OT system in separation-induced maternally directed behavior. We hypothesized that the OT system plays a specific role in social transitions, suggesting that OT neuron activity would be modulated by transition between nonseparation, separation and reunion contexts. We thus assessed the neuronal activation of hypothalamic OT neurons under these conditions. We first labeled the transcription factor c-Fos, an indirect marker for neuronal activity, in PVN and SON sections from P15 pups after 2 hours of maternal separation, and analyzed the selective activation of OT neurons by colocalization of OT and c-Fos immunoreactivity (Fig. 2A). Our results showed increased c-Fos expression in OT neurons both in the PVN and SON of separated pups (Fig. 2B) but not in other stress-associated regions (Fig. 2C), suggesting these changes were not due to global brain activation. This elevated activity was attenuated in pups that underwent 3 hours of maternal separation followed by 1.5 hours of reunion in their home cage (Fig. 2B; "Re").

The elevated activity of OT neurons observed in maternally separated pups was not associated with an increase in peripheral OT concentration (Fig. 2D). We considered the possibility that OT neurons are not yet mature enough to release OT into the circulation at this age. However, intraperitoneal (i.p.) injection of the blood-brain barrier–impermeable retrograde tracer FluoroGold [FG; (*32*)] in P7 pups revealed selective

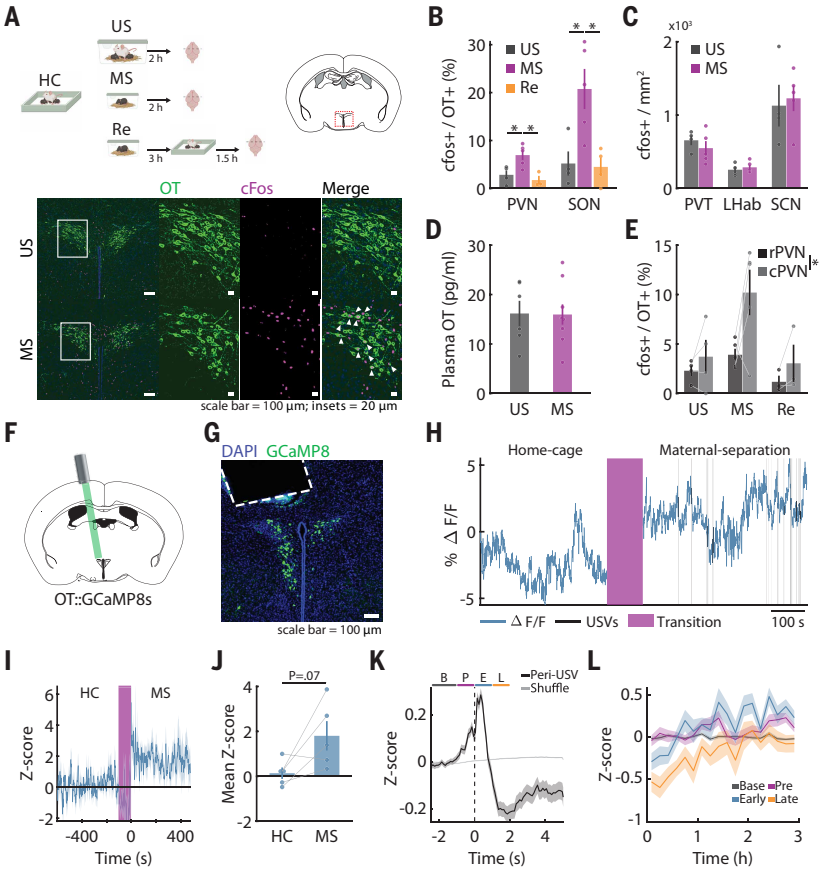

Fig. 2. OT neurons are recruited during maternal separation and are transiently excited during USV bouts. (**A**) (Top) Schematics of the experimental design (MS pups: $n_{(MS)} = 5$; US pups: $n_{(US)} = 4$; reunited pups: $n_{(Re)} = 4$). Red dash indicates the location of the PVN (top right). (Bottom) Representative images of the PVN from US and MS pups. White arrowhead indicates colocalization of OT (green) and c-Fos (magenta). (**B**) OT neurons positive for c-Fos immunoreactivity in the PVN and SON of US (gray), MS (magenta), and reunited pups (orange). One-way ANOVA with Bonferroni-corrected post hoc comparisons. PVN: $F_{groups(2,9)} = 7.981$, $P = 0.01$; SON: $F_{groups(2,10)} = 8.318$, $P = 0.007$. (**C**) Quantification of c-Fos positive cells (normalized to area) in the paraventricular thalamus (PVT), lateral habenula (LHab), and suprachiasmatic nucleus (SCN) for US and MS pups. Student's *t*-test: $t_{PVT(7)} = 0.868$, $P = 0.414$; $t_{LHab(7)} = -0.619$, $P = 0.555$; $t_{SCN(7)} = -0.315$, $P = 0.762$. (**D**) Comparison of plasma OT concentration between US and MS pups. Student's *t*-test $t_{(13)} = 0.063$, $P = 0.951$. (**E**) Quantification of c-Fos positive OT neurons in the rostral PVN (rPVN; $|-0.58: -0.94|$ *mm* relative to bregma) and the caudal PVN (cPVN; $|-1.06: -1.22|$ *mm* relative to bregma) for US and MS pups. Mixed-design RM ANOVA $F_{rostal/caudal(1,9)} = 6.912$, $P = 0.027$; $F_{groups(2,9)} = 5.305$, $P = 0.03$; $F_{groups \times [rostal/caudal](2,9)} = 1.890$, $P = 0.206$. (**F**) Schematics illustrating GCaMP8s fluorescence recording from PVN-OT neurons in P15 pups. (**G**) Representative image showing viral expression of GCaMP8s and fiber optic tip in the PVN (dashed line). (**H**) Representative photometry transients ($\Delta F/F$) during home cage (HC) and maternal separation (MS) conditions, overlaid with individual USVs (black lines) recorded during MS. (**I**) Normalized $\Delta F/F$ [z-scored to HC condition; see (*36*)] over 1-sec bins for individual pups (shades; $n = 5$) and averaged across mice (bold line) during HC and MS conditions. (**J**) Average Z-scored $\Delta F/F$ during HC and MS conditions. Student's *t*-test $t_{(4)} = -2.416$, $P = 0.073$. (**K**) Peri-event time histogram (PETH) of normalized OT calcium signal (black) in 100-ms bins averaged across USV bouts during MS and aligned to bout onset ($N = 4176$ USV bouts in $n = 6$ mice; $n = 1000$ shuffles). OT $\Delta F/F$ during pre-bout (P), early-bout (E) and late-bout (L) periods are z-scored to the baseline period (B) for each USV bout. (**L**) Time course of normalized OT calcium signal associated with the pre-, early- and late-bout periods [as presented in (K)] over 10-min bins during 3-hour MS (z-scored to baseline period per bin). Data are presented as mean ± SEM (error bars or shaded areas), $^*P < 0.05$. In K and L, LME model fitting with post-hoc comparisons of estimated marginal means was used for quantifying differences in OT activity between USV periods and over MS. For detailed statistical information, see table S2.

labeling of magno-OT neurons (FG+/OT+; fig. S4A) and distribution of parvo-OT neurons mainly in the caudal PVN (FG-/OT+), consistent with their distribution in adult mice (*5*). Consistent with the lack of elevation in systemic OT, we found that c-Fos expressing OT neurons were mainly distributed in the caudal PVN (Fig. 2E).

To more directly explore the dynamics of OT neurons during maternal separation, we used fiber photometry to measure GCaMP8s fluorescence (*33*) originating in OT neurons while recording USV emission during separation in P15 pups. To express GCaMP8s in PVN-OT neurons, we injected a Cre-dependent GCaMP8s vector to P0 OT-Cre pups (Fig. 2F) and implanted an optical fiber above the right PVN of GCaMP8s-expressing pups several days before the experiment (P12 to P13; Fig 2G).

Upon removal from their home cage to the separation cage, pups emitted a large number of USVs in a burst-like pattern that persisted for the entire separation period (Fig. 2H and fig. S5). Fiber photometry recordings of the GCaMP8s signal allowed us to track the dynamics of PVN-OT neurons during the transition from the home cage to maternal separation (Fig. 2, H to J), and at a finer scale during the emission of USVs during separation. Alignment of the GCaMP8s signal to the onset of USV bouts revealed a seconds-scale association between these bouts and OT neuron calcium transients during separation (Fig. 2K). Specifically, OT neurons showed ramping activity prior to the USV bout, which peaked immediately after bout onset and declined within seconds (Fig. 2K). To further examine the time course of USV-associated OT transients throughout maternal separation, we assessed how this pattern evolves over time. Whereas Pre-bout OT activity remained mildly elevated compared with the baseline throughout separation, Early and Late-bout OT activity showed a dynamic trajectory—decreasing during early separation but gradually increasing over time, reaching peak in the second half of maternal separation (Fig. 2L and fig. S5). Together, these findings confirm that OT neurons are recruited during maternal separation and suggest that they transiently increase their activity when USVs are emitted, with a progressive increase over time.

Previous work has demonstrated synaptic changes in PVN neurons of adult mice following a brief exposure to a stressor (*34*). Although we were able to identify magno- and parvo-OT subtypes based on previously established electrophysiological signatures [(*5*, *35*); fig. S4, B to D], we found no differences in synaptic input or intrinsic properties of OT neurons from separated pups compared with unseparated controls [fig. S4, E to G; see (*36*)].

Altogether, we show that maternal separation increases the activity of hypothalamic OT neurons. Our results demonstrate that the magno-OT and parvo-OT neurons are anatomically and functionally mature as early as the second week of life in mice and suggest a selective role for parvo-OT neurons in separation.

Blocking OT receptors during maternal separation inhibits maternally directed behavior upon reunion

Having observed increased activity of OT neurons during maternal separation, we next hypothesized that blocking the OTR during maternal separation would alter maternally directed behavior. Systemic injection of

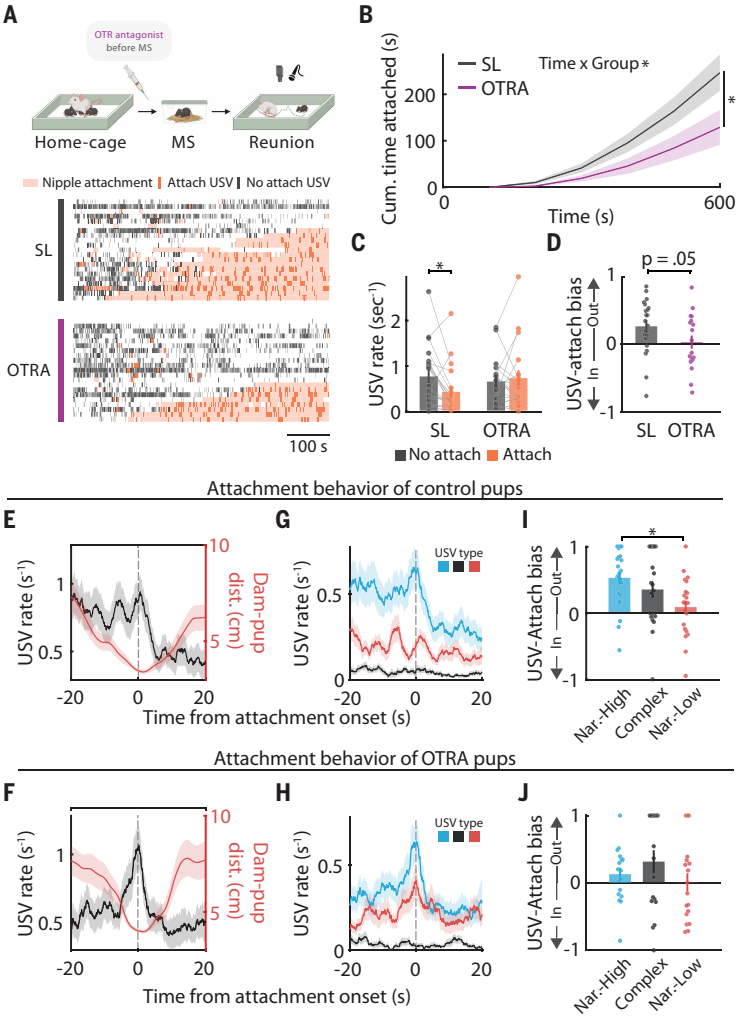

Fig. 3. Blocking the OT receptor during maternal separation suppresses maternally-directed behavior upon reunion. (**A**) Schematic representation of the experimental protocol. P15 pups were treated with OTRA [$n_{(OTRA)} = 21$; i.p.] and compared with vehicle-treated mice [SL; $n_{(SL)} = 21$]. (Bottom) Raster plot depicting USVs emitted by OTRA-treated (magenta) and control (gray) pups, overlaid with bouts of nipple attachment upon reunion with the dam and sorted based on total duration of nipple attachment (ascending). (**B**) Cumulative time of nipple attachment. Mixed-design repeated measures ANOVA $F_{time(1.12,44.811)} = 42.786, P = 1.75 \times 10^{-8}$; $F_{groups(1,40)} = 4.574, P = 0.039$; $F_{time \times groups(1.12,44.811)} = 4.068, P = 0.045$. (**C**) Quantification of USV rate outside (gray) and within (orange) attachment events. Mixed-design repeated measures ANOVA with post-hoc Bonferroni correction $F_{attach(1,37)} = 1.842, P = 0.183$; $F_{groups(1,37)} = 0.299, P = 0.588$; $F_{attach \times groups(1,37)} = 4.565, P = 0.039$. (**D**) The USV attachment bias. Two-sided Mann Whitney U-test $U = 119, P = 0.05$. (**E** to **H**) Temporal dynamics of USV emission around the onset of attachment events for control [$n = 84$ events in 21 mice; (E) and (G)] and OTRA-treated pups [$n = 59$ events in 18 mice; (F) and (H). (E) to (F) Peri-event time histogram (PETH) of average USV rate (black) and MP distance (red) centered at the onset of nipple attachment. (G) to (H) PETH of averaged USV rate of the three USV clusters (as shown in fig. S7) centered at the onset of nipple attachment. Blue trace, narrow bw, high frequency (Nar.-High); black trace, mixed bw, medium frequency (Complex); red trace, narrow bw, low frequency (Nar.-Low). (**I** to **J**) Cluster-specific USV attachment bias for control (I) and OTRA (J) pups. GLMM fitting with Bonferroni-corrected post-hoc comparisons. Data are presented as mean ± SEM (error bars or shaded areas), $*P < 0.05$, $**P < 0.01$. For detailed statistical information, see table S2.

an OTR antagonist (OTRA), 30 minutes before separation, led to a decrease in the total duration of nipple attachment during reunion (Fig. 3, A and B) that could not be explained by changes in event length distribution, attachment event intervals, or the total number of events (fig. S6, A to C).

We next examined the effects of OTRA on USV emission upon reunion. Although we found no difference between OTRA-treated and control pups in the number of USVs (fig. S6D) or in the type of USVs emitted (fig. S7, A, B, D, and E), we identified substantial changes in the physical properties of the vocalizations. Specifically, OTRA pups emitted USVs with higher mean frequency and lower amplitude compared with the control, with no differences in duration or bandwidth (fig. S6, E to H). These findings indicate that inhibition of OT signaling can induce robust changes in nipple attachment and in the properties of emitted USVs, consistent with accumulating evidence demonstrating that USV emission can be modulated by emotional and social states (*29*, *37*, *38*, *39*).

To understand the effect of OTR inhibition on the relationship between USV emission and nipple attachment, we calculated the total USV rate per mouse outside and within attachment events. Control pups displayed a lower rate of USV calls during nipple attachment than outside of attachment events. By contrast, OTRA-treated pups emitted similar numbers of USVs in these two states (Fig. 3, C and D). We next examined the second-scale dynamics of USV emission around the onset of individual nipple attachment events. In both OTRA-treated and control pups, nipple attachment was preceded by a shortening of dam-pup distance (Fig. 3, E and F, and movie S2). In control pups this decrease in dam-pup distance was associated with high USV emission rates, which were rapidly attenuated upon attachment. However, in OTRA-treated pups the USV rate was lower before attachment, increased abruptly around attachment onset, and then declined to pre-attachment rates. Using the classification method described in Fig. 1J, we found that this attachment-associated modulation of USVs was mainly driven by the Narrow-High subset of USVs (Fig. 3, G and H). Quantification of this phenotype revealed that control pups emitted Narrow-High USVs predominantly outside attachment events compared with the Narrow-Low USVs, whereas in OTRA-treated pups this bias was abolished (Fig. 3, I and J).

We also examined more closely USV modulation around the first event of nipple attachment in separated pups after treatment with OTRA. While control pups increased their USV emission rate when approaching the dam, OTRA pups did not show such modulation (fig. S6, I to J). We further found that control pups frequently used Narrow-High USVs before the first attachment, and this USV class rapidly declined after attachment (fig. S7C). This cluster-specific USV modulation was absent in OTRA-treated pups (fig. S7F).

Blocking the OT receptor by injection of OTRA at the end of maternal separation and before reunion with the dam did not affect attachment behavior or attachment-induced modulation of USV emission during reunion (fig. S8). Taken together, these findings indicate that OT signaling during separation plays an important role in maternally directed behavior during reunion.

Development of a method for transcranial optical silencing of OT neurons in postnatal mice

We hypothesized that activation of the OT system and central release of OT during acute maternal separation are involved in modulating maternally directed behavior upon reunion. However, the pharmacokinetics of OTRA treatment did not allow us to dissociate the specific role of OT release during separation from a potential role during reunion. To address this question with higher temporal precision, we developed an optogenetic approach for neuronal silencing in the pup brain.

We hypothesized that eOPN3, a red-shifted and light-sensitive opsin recently developed by our group (*40*), could be well-suited for our scope.

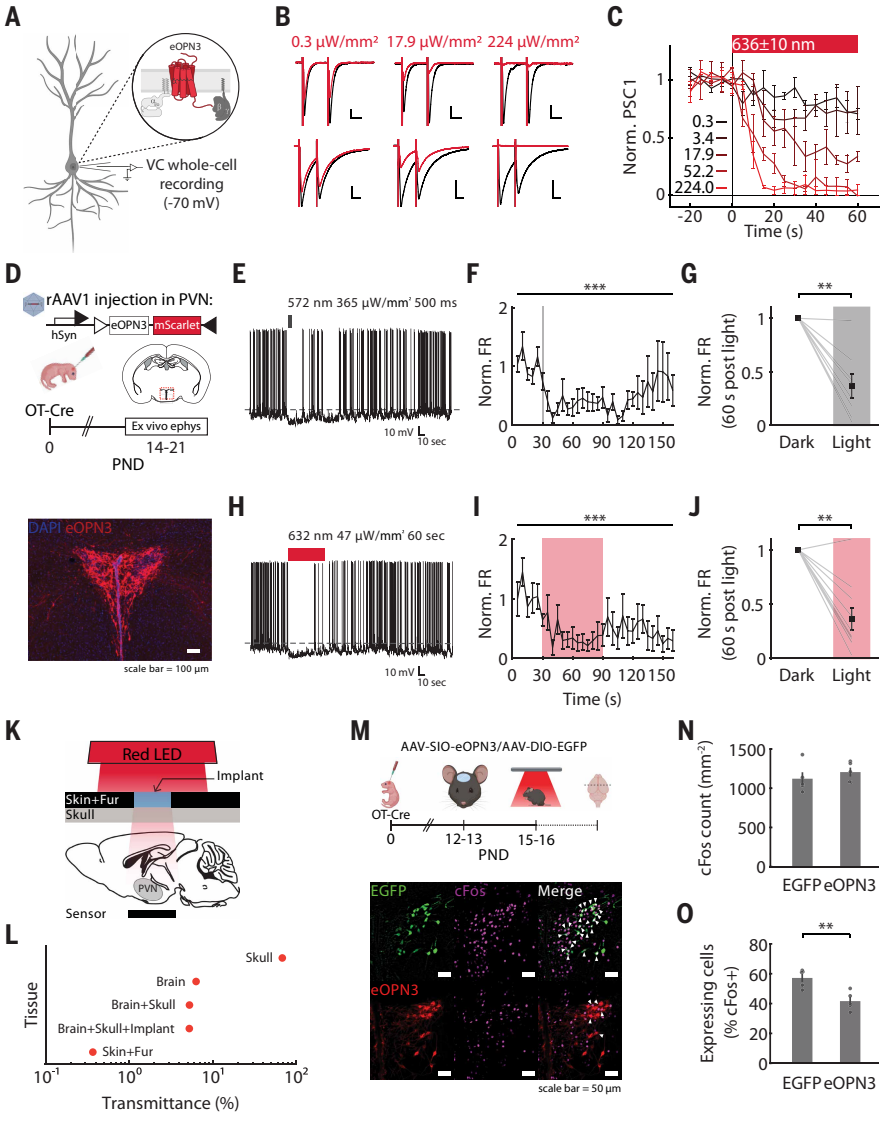

Fig. 4. eOPN3-mediated transcranial photoinhibition of OT neurons in freely behaving pups. (**A**) Schematic illustrating the electrophysiological recordings in autaptic hippocampal neurons expressing the $G_{i/o}$ protein-coupled opsin eOPN3. (**B**) Representative whole-cell voltage clamp recordings from glutamatergic (top) and GABAergic (bottom) neurons of responses to pairs of depolarizing current injections in the dark (black) or during red light illumination (636 ± 10 nm) at three intensities. (**C**) Summary of time course over 5-sec bins, showing postsynaptic currents (PSCs) before and during 60 seconds of illumination at the indicated red light intensities (EC_{50} = 4.6 W/mm^2). Values represent light irradiance in W/mm^2. (**D**) (Top) Schematic of neonatal viral injection and electrophysiological recordings from acute slices of the PVN (dashed line) containing OT-eOPN3 neurons. (Bottom) Representative image showing early (P14) somatic and axonal expression of eOPN3 opsin in PVN-OT neurons. (**E** to **J**) Representative traces (E) and (H), summary of time course over 5-sec bins (F) and (I), and normalized post-illumination comparison (G) and (J) of firing rate in neurons expressing OT-eOPN3 before and after continuous stimulation with green [(E) to (G); $n = 8$] or red [(H) to (J); $n = 10$] light, respectively. (F) and (I) Friedman test for comparison of firing rate over time. $\chi^2_{green(31)} = 77.076, P = 8.49 \times 10^{-6}; \chi^2_{red(31)} = 65.183, P = 3.17 \times 10^{-4}$. (G) and (J) Paired t-test $t_{green(7)} = 5.273$, $P = 0.001$; $t_{red(9)} = 4.053, P = 0.003$. (**K**) Diagram illustrating the characterization of red light penetration through brain tissue. (**L**) Transmittance of red light through the different tissues. (**M**) (Top)Schematic representation of the experimental approach for eOPN3-mediated transcranial silencing of OT neurons in freely moving pups. (Bottom) Representative images of the PVN from OT-EGFP (green; $n = 5$) and OT-eOPN3 (red; $n = 5$) mice co-stained for c-Fos (magenta) after salt loading. Arrowheads indicate the overlap of c-Fos-positive neurons and EGFP- or eOPN3-positive neurons. (**N**) Quantification of c-Fos positive cells in the PVN. Student's t-test $t_{(8)} = -0.847, P = 0.421$. (**O**) Percentage of EGFP- and eOPN3-expressing neurons positive for c-Fos immunoreactivity in the PVN. Student's t-test $t_{(8)} = 4.034, P = 0.004$. Data are presented as mean ± SEM (error bars), $^{**}P < 0.01$ $^{***}P < 0.001$.

We first confirmed that illumination with low-irradiance red light was sufficient to evoke robust reduction in postsynaptic currents in eOPN3-expressing hippocampal neurons in vitro (Fig. 4, A to C), indicating that eOPN3 might serve as an efficient tool for transcranial inhibition in mouse pups.

To examine whether optogenetic silencing with eOPN3 could effectively inhibit neuron activity in PVN-OT neurons in early life, we expressed eOPN3 in OT neurons (Fig. 4D) and conducted electrophysiological whole-cell recordings from eOPN3-expressing OT neurons in acute PVN slices. We confirmed that illumination of eOPN3-expressing cells with green light evoked a potent and reversible reduction in firing rate (Fig. 4, E to G). Consistent with our hippocampal neuron recordings, activation of eOPN3 with low-irradiance red light was also sufficient to evoke a reduction in action potential firing in OT neurons (Fig. 4, H to J). Thus, delivery of low irradiance red light was sufficient to activate eOPN3 and suppress OT neuron activity.

Next, we determined whether we could deliver a sufficient amount of red light to the PVN, located 4 to 4.5 mm below the skull surface in P15 mice, through a minimally invasive optogenetic strategy. We designed a surgical procedure that allowed stable optical access to pups' intact skulls and optimized the amount of light that could reach the PVN (fig. S9A). We then measured the amount of red light transmitted through the brain in this configuration [Fig. 4K and fig. S9, B and C; see (*36*)]. Light transmission through the implant, skull, and brain (transmittance = 5.25%) was similar to transmission through the skull and brain, or the extracted brain only (5.28 and 6.33%, respectively; Fig. 4L). Measuring at different dorsoventral planes of the brain revealed an exponential decay in transmittance as a function of tissue thickness (fig. S9D). Below the ventral surface of the brain in implanted mice, we detected an absolute irradiance of 8.77 W/mm^2. These measurements indicated that a sufficient amount of light reaches the PVN to activate eOPN3 under these conditions.

eOPN3 facilitates transcranial, tether-free photoinhibition of OT neurons in freely behaving pups

Next, we investigated whether the transcranial optogenetic strategy described above could be used to inhibit PVN-OT neurons in preweaning pups in vivo. We expressed eOPN3-mScarlet or EGFP in PVN-OT neurons (Fig. 4M). We then asked whether transcranial red-light illumination could suppress c-Fos immunoreactivity in PVN-OT neurons of salt-loaded pups [fig. S10A; (*41*, *42*)]. Although eOPN3-expressing pups showed no change in the general PVN c-Fos count compared with EGFP-expressing controls, we observed a suppression of c-Fos immunoreactivity in PVN OT-eOPN3-expressing neurons compared with controls (Fig. 4, N to O).

We further confirmed these findings in a separate cohort of animals, in which pups expressing

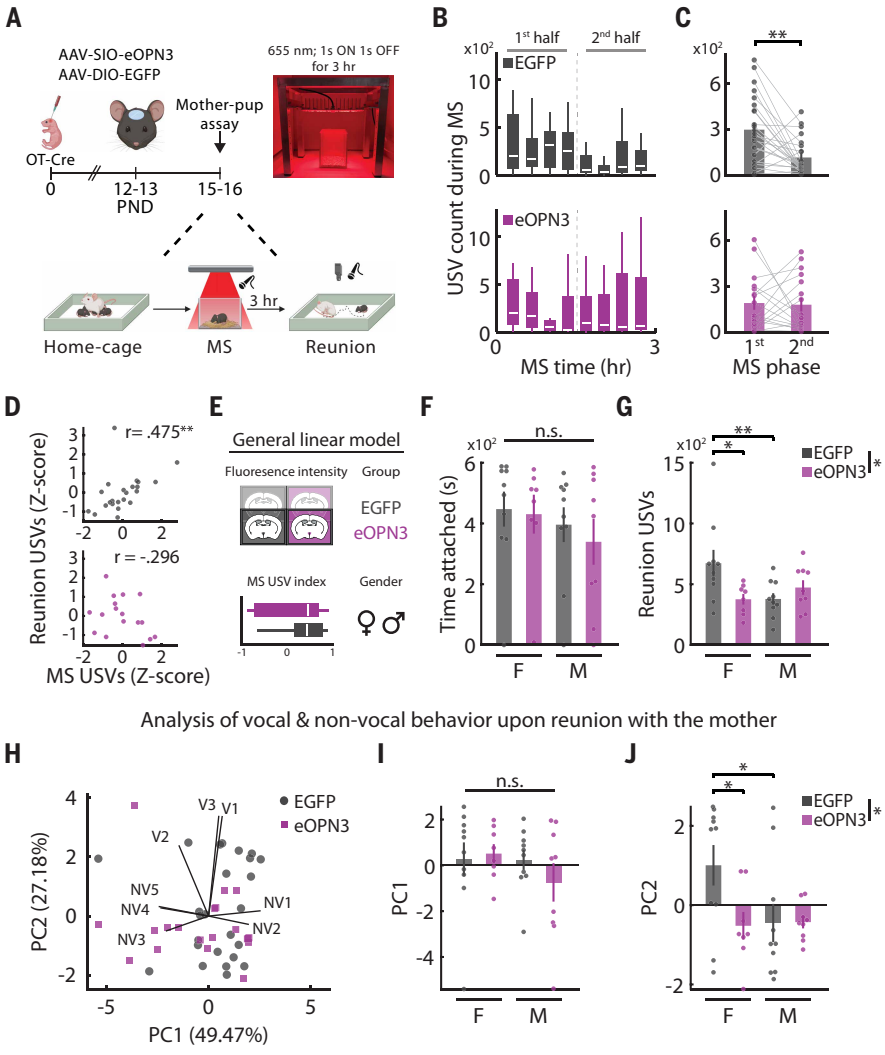

Fig. 5. Optogenetic silencing of OT neurons during MS selectively alters vocal behavior of pups during separation and reunion. (**A**) Schematic representation of the experimental approach, as described in Fig. 4. P15 pups underwent optogenetic silencing of OT neurons during MS [$n_{(OT-EGFP)} = 26$, $n_{(OT-eOPN3)} = 19$]. Image shows the red LED illumination setup. (**B** to **C**) Analysis of USV emission during MS for OT-EGFP (gray; $n = 24$) and OT-eOPN3 (magenta; $n = 17$) pups. (B) USV counts during a 3-hour MS period, recorded in 5-min segments at 15-min intervals. Box plots mark IQR (box edges) and median (white line); whiskers mark 1.5 ± IQR. Mixed-design repeated measures ANOVA $F_{group(1,37)} = 0.012$, $P = 0.912$; $F_{sex(1,37)} = 0.513$, $P = 0.478$. (C) Summary of USV count during the first and second halves of MS. Mixed-design repeated measures ANOVA with post-hoc Bonferroni correction comparing MS phases $F_{phase(1,37)} = 5.955$, $P = 0.02$; $F_{group(1,37)} = 0.245$, $P = 0.624$; $F_{group\times phase(1,37)} = 4.743$, $P = 0.036$. (**D**) Correlation of USV counts during MS and reunion for OT-EGFP (top; Kendall tau coefficient; $P = 0.002$) and OT-eOPN3 (bottom; $P = 0.108$) pups. (**E**) Schematic outline of the general linear model (GLM) used for predicting maternally directed behavior upon reunion for OT-EGFP [$n_{(F)} = 10$, $n_{(M)} = 10$] and OT-eOPN3 [$n_{(F)} = 8$, $n_{(M)} = 9$] pups. The following data are categorized by gender. (**F**) Total time of nipple attachment during reunion with the dam. GLM fitting: $R^2_{adj} = -0.103$; $P_{group} = 0.873$; $P_{sex} = 0.599$; $P_{group\times sex} = 0.759$. (**G**) USV counts during reunion. GLM fitting with post-hoc comparisons of Bonferroni-corrected estimated marginal means: $R^2_{adj} = 0.291$; $P_{group} = 0.012$; $P_{sex} = 0.002$; $P_{group\times sex} = 0.005$. (**H**) Principal component analysis (PCA) of maternally-directed behaviors upon reunion for OT-EGFP and OT-eOPN3 pups. Each data point represents an individual pup, and arrows indicate the projection of non-vocal (NV1-NV5) and vocal (V1-V3) behaviors onto PC1 and PC2. (**I** to **J**) The distribution of PC1 (I) and PC2 (J) fitted to the model. GLM fitting with post-hoc comparisons of Bonferroni-corrected estimated marginal means. For PC1: $R^2_{adj} = -0.086$; $P_{group} = 0.834$; $P_{sex} = 0.985$; $P_{group\times sex} = 0.357$; for PC2: $R^2_{adj} = 0.208$; $P_{group} = 0.024$; $P_{sex} = 0.007$; $P_{group\times sex} = 0.044$. Data are presented as mean ± SEM (error bars), $^{**}P < 0.01$ $^{***}P < 0.001$. For detailed statistical information, see table S2.

eOPN3-mScarlet or EGFP in OT neurons were anesthetized at P15 and underwent continuous illumination via a fiber-coupled red LED placed above the implant (fig. S10B). Although overall PVN activity remained unchanged, red light illumination decreased the activity of PVN-OT neurons in eOPN3-expressing pups compared with EGFP controls (fig. S10, C and D). The expression of eOPN3 in itself did not cause a change in c-Fos counts in the absence of red light illumination, suggesting that this effect was not due to constitutive activity of eOPN3 (fig. S10D). Taken together, these data demonstrate that eOPN3 offers a safe and reliable method for transcranial photoinhibition of OT neurons in untethered, freely behaving pups.

Optogenetic silencing of OT neurons during maternal separation selectively alters vocal behavior during separation and reunion

We next bilaterally expressed eOPN3 or EGFP in hypothalamic OT neurons of OT-Cre pups of both sexes, and used the transcranial approach described above to suppress OT neuron activity during 3 hours of maternal separation at P15 (*36*). We then examined the behavior of pups during separation and reunion with the dam (Fig. 5A). eOPN3 was also expressed in SON OT neurons in 15 out of 19 pups, with high specificity to OT neurons (fig. S11, A to D), indicating that our manipulation selectively targeted the two main hubs of the OT system, which we previously showed are activated during maternal separation.

First, we asked whether OT neuron inhibition during separation would modulate USV emission during separation (MS-USVs). We found that while USV emission spontaneously decreased in OT-EGFP pups over the course of the 3-hour separation period, dropping during the second half of this period (Fig. 5, B and C, top), OT-eOPN3 pups continued to vocalize at a similar rate, with no difference in USV counts between the first and second half of separation (Fig. 5, B and C, bottom). When accounting for sex, our analysis did not reveal differences in USV counts between male and female pups, nor was there interaction with sex (table S2). The overall MS-USV counts for OT-eOPN3 pups were not different from the control pups, indicating that activation of the OT system during separation primarily affects the dynamics of MS-USVs, rather than the total count of USVs, and suggesting a modulatory effect of OT on USV emission during maternal separation.

To further examine this effect, we tested a separate cohort of pups injected with OTRA before maternal separation and compared them with vehicle-treated control pups. Consistent with our optogenetic findings, blocking OTR during separation disrupted the USV emission profile, in particular the spontaneous gradual decline observed in control pups over the separation period (fig. S12A). Although control pups in this experiment displayed a faster decline in USV emission and did not show a drop between the first and second halves of maternal separation—likely due to the less stressful nature of the pharmacological

approach compared with the continuous transcranial illumination—OTRA-treated pups increased their USV emission in the second half of separation (fig. S12B). Taken together, this pattern aligns with our findings of USV-associated recruitment of OT activity that builds up during separation (Fig. 2L and fig. S5), suggesting an OT-mediated mechanism to suppress USV emission during maternal separation.

Based on our previous findings, we then hypothesized that activation of the OT system during maternal separation plays an important role in guiding maternally directed behavior upon reunion. We therefore tested whether optogenetic silencing of OT neurons during separation would alter this behavior. Analysis of USV counts during reunion (Reunion-USVs) revealed that while control pups exhibited a strong positive correlation between MS-USVs and Reunion-USVs, this correlation was absent in pups expressing eOPN3 (Fig. 5D).

Unlike our pharmacological intervention (Fig. 3), silencing of OT neurons during separation did not affect attachment behavior and attachment-associated modulation of USV emission during reunion (fig. S13). Given the well-established role of OT neurons in affiliative behavior and touch, these results led us to hypothesize that selective optogenetic silencing of the OT system during separation differently affect vocal and nonvocal behaviors during reunion. We thus leveraged the rich dataset we collected in the current experimental design and evaluated the extent to which certain features contributed to the variation in behavior upon reunion. Specifically, in addition to the categorical information about the experimental group (OT-eOPN3 versus OT-EGFP) and sex, we analyzed the USV attenuation index during separation and transgene expression in the mouse PVN [fig. S11, E and F; see (*36*)]. We found that none of the predictive features could account for the variance in nipple attachment behavior (Fig. 5F). By contrast, both the experimental group and sex independently predicted Reunion-USVs. Female OT-eOPN3 pups displayed a reduction in Reunion-USVs when compared with female OT-EGFP pups, whereas male OT-eOPN3 pups emitted USVs similar to their control counterparts. Furthermore, although we observed a marked difference in Reunion-USVs between female and male EGFP-OT pups, this sexual dimorphism was absent in OT-eOPN3 pups (Fig. 5G).

We then categorized measurements of pup behavior toward the dam into nonvocal (NV) and vocal (V) behaviors, finding strong correlation within each domain (fig. S14A). Using PCA analysis on behavioral variables recorded during reunion [see (*36*)], we found that nonvocal and vocal behaviors projected onto PC1 and PC2, respectively, which together explained approximately 77% of the variance (Fig. 5H and fig. S14B). Consistent with our previous results, we found that although none of the predictive features could account for the variance in PC1 (Fig. 5I), the variance in PC2 was predicted by both the experimental group and sex. Specifically, female OT-eOPN3 pups, but not male OT-eOPN3 pups, exhibited a difference compared with controls in PC2 (Fig. 5J). Taken together, our findings underscore the critical role of OT neuron activity during maternal separation in shaping vocal, but not nonvocal, behavior during separation and subsequent reunion with the dam. These results suggest a sex-specific contribution of OT neurons to maternally directed behavior in the preweaning period, highlighting an important but unexplored aspect of OT function in early development of social behavior.

Discussion

Our current understanding of the OT system's role in social behavior is derived mostly from studies conducted in the adult brain, in which sensory and social networks are mature (*1*, *43*, *44*). In the present study, we established an experimental framework and optogenetic approach for studying early life social behavior in freely behaving pups, demonstrating that OT neurons are recruited during early life maternal separation and that OT modulates the vocal behavior of pups during both separation and reunion, pointing to a hitherto unidentified role for OT in the infant brain.

We speculated that pup USVs, traditionally studied in the controlled context of social isolation (*31*, *45*, *46*, *47*), might also reflect the pups' motivational drive to interact during reunion (*48*). In our awake-dam assay, separated pups showed a transient increase in high-frequency USVs, suggesting an initial distress response that is rapidly alleviated by maternal interaction. This interpretation aligns with recent work in showing MP reunion immediately activates zona incerta neurons that modulate isolation-associated distress (*49*). Consistent with this notion, we found that maternally separated pups reunited with an anesthetized dam also displayed a robust increase in USV emission upon reunion and continued to vocalize throughout the reunion period. These findings parallel recent studies in adult mice that showed isolation-induced increase in USVs during reunion (*50*–*52*) and suggest that social context modulates USVs throughout the lifespan.

Although nipple attachment behavior itself was indistinguishable in separated and unseparated pups, we did observe distinct differences in their vocalizations across behavioral states and specific emission during attachment events, a phenomenon previously reported in piglets but not in rodents (*53*, *54*). Unbiased classification revealed specific USV profiles linked to distinct aspects of attachment behavior, with separated pups emitting more Narrow-High USVs outside of attachment events, reflecting the spectral properties of the early calls emitted following separation in the awake dam assay. Previous studies reported that USVs in rat pups are associated with different aspects of maternal care (*55*, *56*) and that the dam's presence can buffer USVs in infant rats exposed to acute shock (*23*). Our findings further suggest a homeostatic framework underlying spontaneous vocal communication in the preweaning period. Namely, a dam's presence not only suppresses pups' distress calls but also modulates vocal behavior during the interaction. Our results point to nipple attachment behavior as a potential regulator of USV emission during MP interaction.

The social homeostasis theory points to OT as a key driver of isolation-induced social motivation (*48*, *52*, *57*). However, few studies have delved into the functional responses of OT to acute social isolation at any age, much less so in early life. We found that hypothalamic OT neurons increased their activity during maternal separation, consistent with previous studies showing elevated OT immunoreactivity after acute isolation, and with an important role of OT in isolation-induced rebound in social interaction in juvenile and adult mice (*52*, *58*, *59*). Fiber photometry recording further extended these results, showing a temporally precise excitatory association between USV emission and OT neuronal activity that increased throughout the separation period, suggesting a progressive recruitment of OT cells during separation-driven distress.

Anatomically, we identified an increased activation of caudal PVN OT neurons during separation, suggesting that parvocellular OT neurons, prominent in the caudal PVN, play a role in promoting maternally directed behavior during reunion. This is consistent with a recent study showing that most activated OT neurons during acute social isolation in adult mice are enriched in *Cnr1* (*52*), a molecular marker of parvocellular OT neurons (*5*).

Recruitment of parvocellular OT neurons during maternal separation may contribute to maternally directed behavior through local modulation of the larger magnocellular OT subpopulation (*60*, *61*), or directly through OT release at specific synaptic targets such as the nucleus accumbens (NAc) and periaqueductal gray (PAG), brain regions that regulate social reward and USV emission, respectively (*5*, *37*, *62*). In addition, it has been recently found that separation calls and nipple attachment are independently regulated by agouti-related peptide (Agrp) neurons in the arcuate nucleus (*24*). Our results indicate that parvo-OT neurons might act downstream of Agrp cells (*63*) in controlling maternally directed behavior.

Two lines of evidence in our study support a causal role for OT in separation-induced maternally directed behaviors. Both antagonism of OT receptors in separated pups and optogenetic silencing of OT

neurons altered USV dynamics during separation and reunion, and OT receptor antagonism further affected nipple attachment behavior. These results seem to contrast with recent work showing that OT and OTR knockout rat pups were not defective in USV emission during maternal separation (*64*). However, our results revealed altered dynamics in USV emission rate over the course of the separation period without a change in overall USV count. While differences in these studies might arise from the nature of the perturbation (acute versus chronic) or reflect interspecies variability in OTR developmental expression (*65*, *66*), they also expose a complex and nuanced role of OT signaling in modulating separation-induced USVs in early life. Our results help to resolve previous inconclusive findings regarding the role of OT in maternal separation-induced USVs [reviewed in (*67*)], and underscore the importance of extended observation periods to fully capture OT's influence on early life vocal communication.

Our pharmacological and optogenetic findings reveal the importance of OT signaling not only during separation but also in shaping behavior upon reunion. However, differences emerge between the two manipulations: First, there were subtle differences in the dynamics of USV emission during maternal separation between the two manipulations. Such differences could arise due to the fact that the pharmacology experiments required an i.p. injection shortly before separation, which may compound stress. Second, OTRA administration resulted in alterations in nipple attachment behavior upon reunion, whereas optogenetic silencing during separation did not. These differences might naturally arise as a result of the slow pharmacokinetics of OTRA [half-life of 2 hours; (*68*)], compared with the minutes-scale recovery kinetics of eOPN3. Although our c-Fos results suggest decreased OT neuron activity in separated pups upon reunion, there are inherent limitations in using c-Fos as a proxy for neural activity (*69*–*71*). Along with the potential incomplete penetrance of eOPN3 in the PVN, these findings highlight the complexity of the OT system, suggesting that distinct subsets of OT neurons and their targets contribute selectively to different behavioral domains.

There is no consensus in the literature regarding OT's sex-specific effects (*72*). We showed sex differences in MS-induced vocal communication during reunion but not during separation, consistent with the well-established sex differences in spontaneous and context-dependent vocalizations previously reported in rodents and humans (*50*, *51*, *52*, *73*, *74*). Unexpectedly, we further found that the effect of OT neurons on MS-induced USV emission during reunion was sexually dimorphic, revealing a specific effect in female but not male pups. Several studies have recently found sexual dimorphism in OT-mediated effects on behavior in juvenile rats (*75*, *76*). While our findings suggest that such differences are also present in the preweaning period, further research is needed to fully understand the mechanism underlying these differences.

In conclusion, our results reveal a novel role for OT neurons in driving context-dependent, maternally directed behavior in preweaning mice and emphasize the need to study the mechanisms through which the OT system modulates context-specific behaviors during early life. The new tools described here will encourage further research of the neural circuit mechanisms of behavior during the preweaning age, allowing new insights into the development of social behavior in early life.

Materials and Methods

Animals

Animals used for this study were preweaning male C57BL/6J mice (Envigo) and the following transgenic lines: OT-IRES-Cre [RRID:IMSR_JAX:024234; (*77*)]; Ai9 reporter line [RRID:IMSR_JAX: 007909; (*78*)]. OT-Cre mice were maintained by breeding homozygous males with heterozygous females, and pups for the experiments (OT-Cre$^{\pm}$) were generated by breeding of homozygous males with wild-type C57BL/6J females. For experiments in Figs. 4 and 5 and figs. S4 and S10 to S14, both males and females were used. For in vivo behavioral experiments, pups were cross-fostered with age-matched littermates at P0 to P3 and housed in litters of 5 to 8 pups with ICR foster dams (Envigo). Littermates from single cages underwent surgeries on the same day and were assigned to the experiment or control group such that cages always included mixed groups. Mice were kept in temperature- and humidity-controlled rooms on a 12-hour light–dark cycle with food and water ad libitum. All behavioral experiments were conducted during the dark phase. Experiments at the Charité-Universitätsmedizin Berlin were approved by the Berlin local authorities and the animal welfare committee of the Charité-Universitätsmedizin Berlin, Germany, and were done according to the guidelines stated in Directive 2010/63/EU. All procedures described in this paper were approved by the Weizmann Institute Animal Care and Use Committee (#03460524-1, #07650922-3, #06890821-2, #04950621-3, #08531020-2).

Mother-pup assay

The MP assay was employed to study maternally directed behavior in P15 and P16 mouse pups. This behavioral paradigm allowed us to examine pup behavior toward an anesthetized dam after acute maternal-separation (MS) period. The design of this assay was inspired by previously described behavioral assays (*23*, *24*), with a few modifications. Our assay included a 3-hour MS phase, followed by a synchronous assessment of pups' USVs and physical behavior toward the dam during a 10-minute reunion phase. Prior to the experiment, all pups were cross-fostered with an ICR lactating dam at the same postpartum age. Cross-fostering occurred immediately after neonatal injections at P0 (Fig. 2, F and G, and Fig. 5) or at P2–P3 for naive or pharmacologically treated pups (Figs. 1 and 3). Utilizing ICR foster dams, widely used as recipient dams, significantly facilitated pups' survival and also enhanced the contrast ratio of video recording during MP interactions (dark pup against a white dam).

During the MS phase, P15 and P16 pups were transiently separated from their dam and littermates and individually placed in a small cage with fresh bedding for 3 hours. To maintain the pups' body temperature, cages were transferred to a separate room and placed on heating pads set to 32°C. Age-matched, unseparated control pups were transferred with their dam and littermates to a new cage with fresh bedding and placed back on the rack for 3 hours. Following MS, pups were reunited with the dams for the reunion phase. In the reunion phase, pups were placed in a new cage (501 cm^2 floor area; Tecniplast, GM500) containing soiled bedding from their home cage. An anesthetized ICR dam (100 mg/kg Ketamine, 10 mg/kg Xylazine; i.p.) was positioned in the corner opposite the pup's starting point, nipples facing upward. All behavioral experiments were conducted during the dark phase by a trained experimenter who was blinded to the mouse identity.

Ultrasonic vocalization (USV) recording and quantification

USVs emitted by the pups were recorded in a sound-attenuating cubicle (Med Associates) equipped with an ultrasound-sensitive microphone (CM16/CMPA; Avisoft-Bioacoustics) situated ≈ 30 cm above the cage surface. Data were acquired at a sampling rate of 250 kHz and 16-bit resolution using an UltraSoundGate 416H and an Avisoft-RECORDER software (Avisoft Bioacoustics). Gain was manually adjusted online to prevent signal saturation. USVs were detected using DeepSqueak version 2.6.2 (*79*) using the "All Short Calls" v1 network with the following parameters: high recall, "Chunk length" = 5 sec, "Overlap" = 0.06 sec. We excluded frequencies below 25kHz and above 120 kHz, and detected signals > 150 ms to reduce non-USV noise and artifacts. The performance of DeepSqueak was quantified using the overlap between ground-truth (GT) and predicted USVs (intersection-over-union; S3A). Bounding boxes for individual USVs were manually annotated (n = 802 USVs in 2 mice) by a trained observer and served as GT. Best-predicted fit: $median = 0.905$, $IQR = [0.763 - 0.963]$; best-GT fit: $median = 0.884$, $IQR = [0.664 - 0.958]$.

We employed two classification methods for the detected USVs. First, we used VocalMat classifier (*30*), which uses a supervised learning model to classify the detected calls into a predefined set of vocal classes [adopted from (*31*, *80*)]. We evaluated VocalMat performance by comparing the most likely class predicted by the classifier to the class assigned by a trained observer ($n = 1950$ in 6 mice; fig. S3B). We maximized the overall F1 score of the model by calculating the optimal prediction score (threshold; [0 to 1]) that optimizes F1 measure for each category. In addition, we expanded the analysis to consider one of the two most likely USV types assigned by the model, based on a classification approach of multi-class probability (*30*). This strategy improved the overall accuracy of the model (overall F1 score = 50.3%), mainly for the more prevalent categories. Based on this analysis, we conservatively included in all further analyses vocal classes that could be reliably predicted by VocalMat (*accuracy* > 50%; *chevron*, *down fm*, *flat*, *short*, *step up*, *up fm*). USVs that could not be classified using this method were labeled as *other*.

Additionally, we used the bandwidth and mean frequency of individual USVs to conduct an unsupervised classification of the detected USVs using k-means cluster analysis. Data were standardized to Z-scores and *kmeans* function was employed in MATLAB with 10 replicates to search for a local minimum. To determine the optimal number of clusters for this classification, we employed silhouette analysis using the *silhouette* function in MATLAB. This analysis was done separately for each experimental group.

We further examined the distribution of the predefined vocal categories (VocalMat classifier) in each USV cluster (fig. S2L and fig. S7, B and E). Mice with no USVs in at least one of the clusters were excluded from this analysis.

For the analysis of short- and long-range USVs (fig. S2, F to G, and fig. S6J), we defined the "mother-zone" as a 7-cm radius from the dam's center of mass, setting a threshold for short-range (within the mother-zone) and long-range (outside the mother-zone) USVs. We analyzed the USV rates of short- and long-range USVs before the first nipple attachment. We used the aligned rank transform analysis of variance (ANOVA) (ART; *art* function in R) with Bonferroni-corrected post hoc Wilcoxon signed-rank tests.

Video recording, synchronization and quantification

Top-view videos of the reunion phase were recorded at 25 frames per second (1280 X 1024 resolution) using a GigE monochrome camera (DMK 33GP1300, Imaging Source) attached to a lens (H3Z4518CS-MPIR, Computar) under 850-nm IR illumination for 10 minutes. Videos were recorded using Streampix8 (Norpix, Canada), coupled to a custom Arduino-based system that allowed the acquisition and control of four independent setups simultaneously. An Arduino-controlled LED (1 W, 820 nm) was placed in each camera's field of view and flashed at 0.05 Hz (100 ms pulse width) to facilitate the synchronization of video frames with the audio signal. A TTL-based signal, driven by the same pulse used for the video sync signal, was encoded in the least significant bit of the 16-bit audio sample and synchronized to the video stream via a custom MATLAB script. Automated tracking of recorded videos was performed using a custom MATLAB script, using frame-by-frame threshold-based segmentation and identification of the centroid. Manual analysis of behavior (nipple attachment events) was performed using a custom MATLAB script. All analyses were conducted by a trained observer blinded to the mouse identity.

Analysis of USV emission and its relation to nipple attachment behavior

The "USV-attachment bias" index (Fig. 1K and Fig. 3, and J) indicates the tendency of MS pups to use a specific USV cluster outside (positive values) or during an attachment event (negative values). It was calculated per mouse for total USV counts or specifically for the three USV clusters (k-means cluster analysis) as:

$$UVS\text{-}attachment\ bias = \frac{USV_{out} - USV_{in}}{USV_{out} + USV_{in}} \quad (1)$$

where USV_{out} is the USV rate outside nipple attachment and USV_{in} is the USV rate within nipple attachment. Mice that did not display nipple attachment for the entire trial were excluded from the current and subsequent analysis. To analyze the data, which are inherently bounded between −1 and 1 and can contain values at the extremities, we used Beta regression model (GLMM) with a logit link function. To meet the assumptions of Beta regression: (1) We adjusted extreme values (−1 and 1) by adding/subtracting a small constant (epsilon = 10^{-5}) to avoid computational issues in the Beta distribution. (2) We rescaled the data to fit the Beta model's required range $(0, 1)$:

$$y' = \frac{y + 1}{2} \quad (2)$$

This preserved the meaningful distinction between the original negative and positive values of our index while making the model statistically valid. We then fitted a GLMM (*glmmTMB* function in R) with: (1) Fixed effects for group (*grpID*), USV cluster (*clusterID*), and their interaction (*grpID* * *clusterID*). (2) A random intercept for *mouseID*, accounting for repeated measures within subjects. The GLMM is structured as follows:

$$UsvAttachBias \sim grpID \times clusterID + (1 \mid mouseID) \quad (3)$$

For the analysis of cluster-specific USV emission in relation to the first nipple attachment (Fig. 1L and fig. S7, C and F), we calculated the Z-score distribution of USV rate per mouse for each cluster over 60-second time bins. These time bins were aligned to the time of first nipple attachment and averaged across mice. We presented the nine time bins that included the highest number of mice per group. Importantly, our statistical model includes all available time bins per mouse and accounts for missing values at the extremities of the timeline.

For the analysis, we used a linear mixed-effect model (LME; *lmer* function in R). Our model included fixed effects for group (*grpID*), USV cluster (*clusterID*) and time in relation to first attachment (*normTime*) and their interactions. We also included random intercept for mouseID, accounting for repeated measures within subjects, and a random slope for normTime accounting for individual differences in time trends. We fitted the model using the following formula:

$$ClusterUsv1stAttach \sim grpID \times clusterID \times normTime + (normTime|mouseID) \quad (4)$$

We used FDR-corrected multiple comparisons of estimated marginal means to compare cluster-specific differences within each time bin. Notably, the behavioral results in naive pups (Fig. 1, K to L), along with the overall lower number of Complex USVs in similar analyses (table S1), led us to hypothesize that the association between USV emission and nipple attachment behavior is mainly driven by Narrow-High and Narrow-Low USVs. We therefore focused our subsequent statistical models on these two USV types.

To study the temporal dynamics of USV emission in relation to the onset of nipple attachment (Fig. 3, E, G, F, and H), we pooled together attachment events for each experimental group and analyzed the USV rates aligned with the onset of events. The USV data were discretized into 100-ms bins, and smoothed using a moving average (window size = 30 bins). Peri-event time histograms (PETHs) were averaged across attachment events, both for total USV counts and for the three specific USV clusters, spanning from −20 to +20 seconds from nipple attachment, and binned at 100 ms intervals. The results were also superimposed with the MP center-of-mass distances, calculated in 100-ms bins and smoothed using a moving average (window size = 30 bins).

Mother-pup assay with an awake mother

For the experiment with an awake dam (Fig. 1, A to D), pups were reunited with their dams in their home cages. Upon reunion, the dam was first returned to the home cage, followed by the pup. All pups were placed in the same corner of the cage, regardless of the dam's position. Mother and pup behaviors were then recorded for the 10-minute reunion phase, using the same set-up as in the anesthetized dam variation of the MP assay. A habituation stage was included to control for the effects of cage-change stress on mother and pup behaviors. On P14, one day prior to the experiment, each dam and her litter were placed in a new cage within the experiment room. Immediately following habituation, dams and litters were returned to their home cages.

A DeepLabCut (v2.2.3) multi-animal neural network (*81*) was used to automatically estimate mother and pup poses over the reunion phase of the MP assay. Mother and pup were labeled on their body centroids. 400 labeled frames, from 10 different pilot experiment videos, were used to train the network. Training was completed over 200,000 iterations, and the model achieved an average error of 3.0 pixels on training images and 6.19 pixels on test images. Centroid labels were used to determine MP distance over each video frame using a custom MATLAB script.

K-means analysis, using the same clustering and silhouette analysis parameters as in the anesthetized dam MP assay, was conducted on combined USV data from experimental and control animals from the first 60s seconds of MP reunion. Clustering data from each group were then plotted on separate graphs.

USV rates (calls/second) over the course of the reunion were analyzed for USVs recorded during the awake mother MP assay. Plotted USV rates were averaged over 1 second bins and smoothed with a 10 second window. Mean USV rates were also plotted against corresponding mean MP distances (cm) over 1 second time bins over the course of the reunion. We fitted a quadratic mixed-effects model (QME) to the data (USV rates for all frequencies, and USV rates above 70kHz mean frequency) to account for nonlinear traits in USV rate over time. This QME incorporated: (i) A main effect of *Group*, (ii) A linear effect of *Time*, (iii) A quadratic effect of *Time*, (iv) Interactions between *Group* and both *Time* and $Time_2$, (v) A random intercept for *mouseID*, accounting for repeated measures within subjects. The model is structured as follows:

$$USVCount \sim Group \times Time + Group \times Time^2 + (1 \mid mouseID) \quad (5)$$

We conducted change point analysis (MATLAB *findchangepts* function) to identify when mean USV rates shifted over time in US, MS, and combined US+MS conditions. Change points were detected at 85 (US), 53 (MS), and 54 seconds (combined data), and the similarity in change points between MS and combined data suggest that shifts in MS vocalization patterns drive the overall USV rate dynamics. Given that MS USV rates decline significantly faster than those of US dyads, we focused subsequent USV analyses on the first 60 seconds to better capture MS-specific vocal changes.

Pharmacological study in vivo

Oxytocin receptor antagonist (OTRA; L-368,899; Tocris 2641) was dissolved in saline 95% and DMSO 5%. We applied 10 mg/kg OTRA intraperitoneally 30 minutes before maternal separation (Fig. 3) or 45 minutes before reunion (fig. S8) in a volume of 10 ml/kg mouse weight. Control animals were injected with vehicle solution containing saline 95% and DMSO 5%. Mice were assigned randomly to OTRA or control groups and litters contained mixed groups.

Primary dissociated hippocampal neuron culture and gene delivery

Autaptic primary hippocampal neuronal cultures on glial cell microislands were prepared from P0 mice (C57BL/6NHsd; Envigo) of either sex as previously described (*82*). 300 m diameter spots of growth-permissive substrate consisting of 0.7 mg ml-1 collagen and 0.1 mg ml-1 poly D-lysine were applied with a custom-made stamp on agarose-coated coverslips. First, astrocytes were seeded and allowed to proliferate in Dulbecco's modified eagle medium (DMEM) supplemented with 10% fetal calf serum and 0.2% penicillin/streptomycin (Invitrogen) for one week to form glia micro-islands. After changing the medium to Neurobasal-A supplemented with 2% B27 and 0.2% penicillin/streptomycin, hippocampal neurons prepared from P0 mice were added at a density of 370 cells/cm^2. rAAV2/1 particles expressing eOPN3-mScarlet under the CaMKIIα promoter were produced in accordance with the protocol described in (*40*). Neurons were transduced with rAAV2/1-CaMKIIa-eOPN3-mScarlet (1.5×10^8 VG per well) at DIV 1 and were recorded between DIV 14 and DIV 21.

In vitro electrophysiology

EPSCs from autaptic primary neurons were recorded under visual guidance using an Olympus IX51 inverted microscope with an Olympus UPlanSApo 20x/0.75 UIS2 objective under infrared widefield illumination. A CoolLED P4000 served as a light source to identify expressing cells and for light activation of eOPN3. To avoid pre-activation of eOPN3 by fluorescence excitation light, electrophysiological recordings were performed first, and cells were only then investigated for expression. Acquired data was excluded in case cells were not expressing. The activation light was filtered with a narrow bandpass filter (center wavelength 636 ± 10 nm, #65-106, Edmund Optics) and additionally attenuated with a 6.0 neutral density filter. Light intensities were measured with a calibrated S130VC power sensor (Thorlabs). Autaptic neurons were constantly perfused with extracellular solution (in mM): 140 NaCl, 2.4 KCl, 10 HEPES, 10 D-glucose, 2 $CaCl_2$, and 4 $MgCl_2$ (pH was adjusted to 7.3 with NaOH, 300 mOsm). Cells were patched with microelectrodes pulled from quartz glass capillaries (3 to 4 MΩ), filled with (in mM): 136 KCl, 17.8 HEPES, 1 EGTA, 0.6 $MgCl_2$, 4 MgATP, 0.3 Na_2GTP, 12 Na_2 phosphocreatine, 50 U/ml phosphocreatine kinase (300 mOsm); pH adjusted to 7.3 with KOH. A Multiclamp 700B (Molecular Devices) amplifier and NI USB-6343 digitizer (National Instruments) were used to control and acquire electrophysiological recordings and the application of light stimulation via WinWCP 5.7 software (https://github.com/johndempster/WinWCPXE). Data was acquired at 10 kHz and filtered at 3 kHz. Cells were kept at −70 mV, and series resistance and capacitance were compensated by 70%. EPSCs were elicited by a 1 ms depolarization to 0 mV (50 ms interstimulus interval, every 5 s), resulting in an unclamped axonal action potential causing neurotransmitter release. Experiments were performed at room temperature. Data were analyzed using Clampfit 10.7 (Molecular Devices). Cells were excluded from analysis if the first EPSC amplitude was below 100 pA, if the access resistance was above 20 MΩ, or if the holding current exceeded 200 pA. All data points represent measurements from biological replicates.

Acute slice electrophysiology

Recordings were performed from acute coronal slices prepared from pups between P14 and P21 (see below). For recording OT neuron activity after maternal separation and electrophysiological identification of magnocellular and parvocellular OT neurons (Fig. 2, A to F), we used an OT-IRES-Cre driver line crossed to a Cre-dependent TdTomato reporter line (OT-IRES-Cre x Ai9). For eOPN3 activation measurements (Fig. 4, D to K), we used OT-IRES-Cre pups injected at P0 into the PVN with a Cre-dependent rAAV2/1 vector expressing eOPN3 (pAAV-hSyn1-SIO-eOPN3-mScarlet-WPRE; Addgene #125713).

Acute brain slice preparation

Pups were injected with pentobarbital (100 mg/kg, i.p.). After decapitation, 300 m-thick coronal slices containing the PVN were prepared in carbogenated (95% O_2, 5% CO_2) ice-cold slicing solution containing (in mM): 2.5 KCl, 11 glucose, 234 sucrose, 26 $NaHCO_3$, 1.25 NaH_2PO_4,

10 $MgSO_4$, 2 $CaCl_2$; pH 7.4, 340 mOsm. Slices were cut using a vibratome (Leica VT 1200S) and allowed to recover for 20 min at 33°C in carbogenated high osmolarity artificial cerebrospinal fluid (aCSF, high-Osm) containing (in mM): 3.2 KCl, 11.8 glucose, 132 NaCl, 27.9 $NaHCO_3$, 1.34 NaH_2PO_4, 1.07 $MgCl_2$, 2.14 $CaCl_2$; pH 7.4, 320 mOsm. Subsequently, slices were incubated for 40 min at 33°C in carbogenated aCSF containing (in mM): 3 KCl, 11 glucose, 123 NaCl, 26 $NaHCO_3$, 1.25 NaH_2PO_4, 1 $MgCl_2$, 2 $CaCl_2$; pH 7.4, 300 mOsm. Finally, slices were kept at room temperature (23°C to 25°C) in the same solution until use.

Whole-cell patch-clamp recording

OT neurons in the PVN were patched under visual guidance using infrared differential interference contrast (DIC) microscopy (BX51W1, Olympus) and an Andor Neo sCMOS camera (Oxford Instruments). Borosilicate glass pipettes (BF100-58-10, Sutter Instrument, Novato, CA, USA) with resistances 4 to 6 MΩ were pulled using a laser micropipette puller (P-2000, Sutter Instrument) and filled with intracellular solution (in mM): 135 potassium-gluconate, 4 KCl, 2 NaCl, 10 HEPES, 4 EGTA, 4 Mg-ATP, 0.3 Na_2-GTP, 10 phosphocreatine-Na_2, 280 mOsm, pH adjusted to 7.3 with KOH. Somatic whole-cell voltage-clamp recordings (>1 GΩ seal resistance, −70 mV holding potential) were performed using a Multiclamp 700B amplifier (Molecular Devices). Data were acquired using pCLAMP 10.7 on a personal computer connected to the amplifier via a Digidata-1440 interface (sampling rate: 20 kHz; low-pass filter: 4 kHz) and analyzed with Clampfit 10.7 (all Molecular Devices). Data obtained with a series resistance > 20 MΩ were discarded. All experiments were conducted at room temperature. In the recording chamber, slices were superfused with carbogenated aCSF (4 to 5 mL/min flow rate). Data were analyzed using Clampfit 10.7 (Molecular Devices).

OT neuron activity after maternal separation

We tested the effect of a 3-hour MS on PVN-OT neurons intrinsic membrane properties ($n = 19$) as well as on their excitatory and inhibitory synaptic inputs (sEPSCs: $n = 18$; sIPSCs: $n = 17$ in 5 mice). We used aged-matched undisturbed pups as controls (intrinsic properties: $n = 14$; sEPSCs: $n = 14$; sIPSCs: $n = 13$ in 4 mice). PVN-OT neurons were identified by the endogenous expression of tdTomato (OT-IRES-Cre x Ai9). As for intrinsic membrane properties, the membrane resistance (Rm), time constant (τm), rheobase and cell excitability were measured. For this, OT neurons were recorded in current-clamp mode at a resting potential of −65 mV. A slow current ramp was applied to the cell to calculate the rheobase, while for Rm, τm and cell excitability, a succession of square pulses was applied (from −20 pA to +40 pA, 5 pA steps). Rm and τm were measured during hyperpolarizing pulses, while the number of AP was plotted for each depolarizing step for cell excitability. Afterwards, spontaneous excitatory (sEPSCs) and inhibitory (sIPSCs) postsynaptic currents were recorded in voltage clamp mode (holding −70 mV for sEPSCs and 0 mV for sIPSCs), and the amplitude and frequency were measured.

OT-eOPN3 activation measurements

PVN-OT neurons were identified by the viral expression of mScarlet (AAV-hSyn-SIO-eOPN3-mScarlet). Cells were recorded in current clamp mode at their resting membrane potential if spontaneously active. In cells that did not spontaneously spike, a small constant depolarizing current was applied to reach a stable low firing rate. Light was delivered using a Lumencor SpectraX light engine, using band-pass filters at 572/35 and 632/22 nm (peak wavelength/bandwidth). The effect of eOPN3 activation on neuronal firing by a long (60 sec) pulse of low intensity red light (632 nm at 47 W/mm^2) was compared to the previously described illumination protocol (*40*) with a brief (500 ms) pulse of green light (572 nm at 365 W/mm^2). For the comparison of post-illumination firing rate in OT-eOPN3 neurons, the values presented are normalized to mean firing rate within a 30-s baseline period and averaged across cells (Fig. 4, F and I).

Classification of magno-OT and parvo-OT neurons

For the classification of magno-OT and parvo-OT neurons, we used both the morphological features of the cells and the electrophysiological protocol previously described (*5*, *61*). Briefly, each cell was hyperpolarized to −100 mV and then depolarized using current steps of increasing amplitude. To discriminate between magno-OT and parvo-OT neurons, we measured the full width at half maximum of the first action potential (AP duration) and the latency to the first action potential.

Stereotaxic injection of AAV vectors

Neonatal stereotaxic injections were conducted as described previously (*83*), with a few modifications. Due to the lack of a standard procedure for neonatal injections into the PVN, we first performed a pilot study to determine the optimal coordinates for PVN injections in newborn mice, as well as the viral serotype and volume of virus required for appropriate viral expression in OT neurons (data not shown). These parameters were used in the following procedure. Briefly, newborn pups were injected after birth (P0), after they had started nursing (6 to 12 hours after parturition). Pups were anesthetized via hypothermia and placed in a stereotaxic apparatus (David Kopf Instruments) using a custom neonatal stage with soft ear bars and a reservoir for ice to maintain anesthesia throughout the procedure. To avoid direct contact with ice, pups were covered with a piece of a nitrile glove. The sagittal and transverse sinuses, clearly visible through the skin at this age, were used as landmarks for our injections, and we defined their intersection as lambda. The anesthetized pup's head was disinfected with 70% ethanol. A Nanofil syringe (World Precision Instruments) with a 34G beveled needle was filled with AAV suspension. The needle was inserted through the scalp and skull into the PVN, bevel facing anterior, and left in place for 1 minute, followed by slowly injecting 300 nL or 500 nL of the virus (100 nL/min). After injection, the needle was left in place for an additional 2 minutes and then slowly withdrawn. PVN coordinates in mm relative to lambda: AP: 2.3, ML: ± 0.35, DV: −2.9. The DV coordinate was zeroed under the skin. The duration of the entire procedure did not exceed 30 minutes. After completing injections in both hemispheres, pups were placed on a heating pad and monitored until their skin color and movement returned to normal. Then, pups were marked with a paw tattoo for identification (Ketchum Manufacturing Inc.). After recovery, pups were cross-fostered with experienced ICR dams, widely used as recipient dams, and closely monitored for their well-being.

The titers of Adeno-associated viral (AAV) vectors used for intracranial injections are *after* dilution in sterile PBS x1 and presented in genome copies per milliliter (gc/ml). AAV vectors in this study included: AAV1-CAG-FLEX-jGCaMP8s-WPRE (1.9×10^{13} gc/ml; Addgene; plasmid #162380), AAV1/2-hSyn1-dlox-jGCaMP8s(rev)-dlox-WPRE-SV40p(A) (8×10^{12} gc/ml; ETH-Zurich; #v627-1), AAV1-hSyn1-DIO-EGFP (7.3×10^{12} gc/ml; Addgene; plasmid #50457), AAV1-hSyn1-SIO-eOPN3-mScarlet-WPRE (7.3×10^{12} gc/ml; Addgene; plasmid #125713). For all experiments, pups were tested at least 14 days after viral injections.

In vivo fiber photometry

Fiber optic implantation: To record OT neuronal activity using fiber photometry, P0 OT-Cre pups were injected stereotactically with AAV-hSyn-DIO-GCaMP8s or AAV-CAG-FLEX-GCaMP8s to target OT neurons in the right PVN. At P12 to P13, pups were removed from their home cage and placed on a heating pad while awaiting the surgery. Pups were anesthetized with isoflurane (induction: 5%, 500 ml/min; maintenance: 0.5 to 1.5%, 50 to 60 ml/min in 100% oxygen; SomnoSuite, Kent Scientific), using a custom mask suitable for stereotactic surgeries in mouse pups. Once the pups were fully sedated, ophthalmic ointment was applied, the hair on the scalp was removed (Veet cream), and pups were immobilized in a Kopf stereotaxic apparatus using modified soft ear bars. Pre-operative analgesia was administered via s.c. buprenorphine, (0.05 mg/kg) and a mix of lidocaine (0.1%) and

bupivacaine (0.025%) at the incision site. The scalp was disinfected with ethanol 70%. A small incision was made along the midline of the scalp, and the skull was cleaned and dried. A craniotomy was performed above the right PVN using a high-speed microdrill (0.5 mm diameter burr bit). A fiber-optic cannula (400 μm core diameter, 0.5 NA, 5.5 mm length; RWD) was lowered to the depth of the PVN in a 10° angle (AP: −0.8 mm; ML: 1.1 mm; DV: −4.7 mm from bregma) and secured in place using C&B Metabond (Parkell). Following implantation, pups were allowed to recover on a heating pad before being returned to their home cage. Post-operative care included monitoring for distress, and administering Carprofen every 24 hours. To acclimatize the pups to the test environment and minimize stress during photometry recordings, implanted pups were habituated to handling and tethering in the testing box for 1 to 2 days before the experiment.

Fiber optic data acquisition: At P15-P16 pups ($n = 6$ of both sexes from 6 litters) were removed to the testing box in their home-cage (with dam and littermates) for 1 hour before the photometry recording. Pups were recorded in their home-cage (with littermates) for 10 minutes. For the MS condition, pups were then removed to a plexiglass cage (10 cm × 8 cm × 14 cm) with fresh bedding, placed on a heating pad, for 3 hours. We simultaneously recorded USVs emitted by the pups during MS. For two pups we sampled 10-min recordings at 30-min intervals, for a total of 6 recording sessions. Four pups were continuously recorded for the 3-hour separation.

Fiber photometry data were acquired using pyPhotometry (*84*) and Doric Fluorescence MiniCube (Doric, Canada), at a sampling rate of 30 Hz, with a 470 nm LED for the calcium signal and a 405 nm LED for the isosbestic signal, illuminated at pulsed mode. The optical system was connected to the pups' cannula through a pigtailed fiber optic rotary joint (400 μm, 0.57 NA; Doric, Canada) and an optical fiber (400 μm, 0.5 NA; RWD). To synchronize the photometry signal with USV emission and video, a TTL-based signal, driven by the same pulse used for the video sync signal and encoded in the least significant bit of the 16-bit audio samples, was sent to pyPhotometry digital input and synchronized via a custom MATLAB script.

Fiber optic data analysis: Raw photometry data were extracted using pyPhotometry package (*data_import* function; source code available at https://github.com/pyPhotometry/code) and pre-processed using pMAT toolbox (*85*). Briefly, the raw signal (GCaMP) was smoothed to reduce high-frequency noise, the control signal (isosbestic) was scaled based on least-squares regression between signal and control, ΔF/F was calculated as [signal-scaled control]/scaled control, and then normalized (robust Z-score) as

$$\left[\Delta\text{Fevent} - median(\Delta\text{Fbaseline})\right] / mad(\Delta\text{Fbaseline}). \quad (6)$$

For the analysis of OT neuron activity during the transition from home-cage to MS conditions, ΔF/F was normalized to 8 minutes during home-cage condition (baseline), and we compared the normalized signal averaged over 8 minutes after the start of MS ("MS") to the normalized signal average over the baseline period ("HC"). One mouse was excluded from the analysis due to missing data during the transition to MS ($n = 5$).

For the analysis of OT activity in relation to USV emission during MS, we calculated peri-event time histogram (PETH) of normalized ΔF/F aligned to USV onset. We detected bouts of USV emission during MS, defined as ≥ 1 USVs with ≤ 0.75 s inter-USV interval (*86*), and analyzed ΔF/F 2.5 s before and 5 s after USV bout onset. USV bouts with ≤ 2.5 s inter-bout interval were excluded from the analysis. ΔF/F was normalized to the 1.5 s before USV bout onset (baseline; −2.5 s to −1 s from onset), and we compared the median Z-scored signal over the "Pre-bout" period (-1 s to 0 s), "Early bout" (0 s to 1 s) and "Late-bout" (1 s to 2 s) to the median Z-scored signal over the baseline period. For the robustness of our analysis we generated time-shifted timestamps using a random interval from the valid USV bouts used for the PETH and computed PETH for each shuffled set ($n = 1000$ shuffles).

For the statistical analysis, we used an LME model. Our model included fixed effects for the bout periods (*periodID*), USV bout onset time (*boutStartTime*) and their interactions. We also included a random intercept for *mouseID*, accounting for repeated USV bouts within subjects. We fitted the model using the following formula:

$$Z\text{-}scored(\Delta\text{F/F}) \sim periodID \times boutStartTime + (1|mouseID) \quad (7)$$

We used Bonferroni-corrected comparisons of estimated marginal means to compare differences between time periods.

Intact-skull implantation and transcranial illumination

For transcranial activation of eOPN3, we designed a minimally invasive surgical procedure that allows optical access to the pups' brain using a 5 mm diameter glass implanted onto the intact skull. P12-P13 pups were removed from the home-cage and placed on a heating pad while awaiting the surgery. Pups were anesthetized with a combination of anesthetic drugs (Medetomidine 0.5 mg/kg; Midazolam 5 mg/kg; Fentanyl 0.05 mg/kg; i.p.), a well-established anesthetic technique in neonatal mice [> P2; (*87*)]. Once the pups were fully sedated, ophthalmic ointment was applied, the hair on the scalp was removed, and pups were immobilized in a Kopf stereotaxic apparatus using modified soft ear bars. The scalp was disinfected with ethanol 70%. A midline incision (8 mm long) was performed in the skin to allow an access to the skull, starting from the anterior edge of the ears (above lambda) to the posterior part of the eyes. Circular excisions were made over the left and right hemispheres of the skull, and the exposed skull was cleaned with sterile saline (NaCl 0.9%) and dried off with a cotton-tipped applicator. Then, a 5 mm glass implant was glued to the exposed skull with cyanoacrylate (Krazy-Glue) and centered over the skull midline with posterior edges around lambda. C&B Metabond (clear; Parkell) was applied to the outside perimeter of the window, covering any exposed bone to ensure a complete seal with the surrounding skin and muscles. The implant is composed of two layers of round coverglass (5 mm, no. 1 thickness; Hecht Assistent) glued together with Norland Optical Adehesive No. 81. (NOA 81; Edmund Optics). After the glues are completely dry, the pups are administered with anesthetic antagonists (atipamezole 2.5 mg/kg; flumazenil 0.5 mg/kg; naloxone 1.2 mg/kg; s.c.) and postoperative analgesia (Carprofen 5 mg/kg; s.c.) and removed back to the heating pad. The entire procedure did not exceed 20 minutes. Once the pups fully recovered, they were returned to their dam and closely monitored until the experiment. Pups with an intact-skull implant showed minimal damage to the skull and brain tissue, displaying high rates of successful recovery from the surgical procedure and long-term survival when monitored up to weaning.

To measure eOPN3-induced changes in PVN-OT neuron activity in vivo, we delivered red light through the intact-skull implant of P15-P16 pups using two different light sources placed above the implant. For experiments that involve measurements in anesthetized pups (0.5% − 1% isoflurane; fig. S10, B to D), an optical fiber (500 m diameter, NA 0.73) was placed above the implant, and pups were illuminated with red LEDs (630 nm; 255 μW/mm^2 at the fiber tip; Prizmatix). For experiments that involve measurements in freely behaving pups (Fig. 4, N to P), a custom 64-Watt red LED array (peak: 655 nm; 20 cm X 10 cm; Zeal-Tech Industries, India; fig. S9C) was installed at a distance of 20 cm above a clear plexiglas cage (10 cm X 8 cm X 14 cm) with a single mouse, providing an irradiance of 191 μW/mm^2 at head level. In both experiments we used a continuous illumination protocol for 80 minutes. Five minutes after red light activation, pups were administered with hyperosmotic solution (salt-loading; see below), and 90 minutes later, pups were euthanized for histological examination. Importantly, with these conditions, we did not observe any evidence of overheating and damage to the brain tissue.

We used the 64-Watt LED array to evaluate the amount of light that could travel through the tissue to reach the PVN. P15-P16 implanted pups were euthanized and decapitated. We removed the upper palate and carefully dissected out the pituitary gland to expose the ventral hypothalamus (fig. S9B), where a light sensor (S130C; 3 mm diameter active area; Thorlabs) was placed for further measurements. The red LED array was installed 20 cm above the testing surface and we calculated light transmission through the following tissue samples: intact-skull implant with brain and skull, brain and skull (skin removed), extracted brain only, skin with fur and skull only. We observed low transmission of red light through the mouse skin and fur (0.37%) and high transmission through the isolated skull (68.1%), supporting our surgical approach (Fig. 4L).

For the assessment of red light penetrance at different dorsoventral levels of the brain, we sectioned the brains in the horizontal plane and calculated the light transmittance through tissue of varying thickness ($3-6$ mm; 1 mm interval). To prevent false detection from ambient light and reflections, tissue samples were covered with aluminum foil, leaving a 5 mm window around the implant. The transmission percentage (T%) of red light was calculated using the formula $T\% = \left(\frac{I_t}{I_0}\right) \times 100$, where I_t is the intensity of light after passing through the tissue and I_0 is the baseline light intensity without any tissue between the sensor and light source. Notably, the light power measured at ventral surface of the brain corresponded with an irradiance of 75μW/mm^2 delivered by a fiber-coupled red LED (630 nm; Prizmatix) placed right above the implant. Consistent with previous work (*88*), we did not observe any evidence of overheating or photodamage to the brain tissue under these illumination conditions.

Salt loading

We used acute salt loading as a method to induce robust c-Fos expression in hypothalamic OT neurons, a well-established procedure as previously described (*41*, *42*). To validate the effectiveness of this approach in pups, P15 pups were injected with hyper-osmotic solution (NaCl 9%; 20 ml/kg mouse weight, i.p.) and compared to pups injected with normal saline (NaCl 0.9%). Pups were sacrificed 90 minutes after salt loading, and we assessed the expression patterns, as depicted in fig. S10A. Subsequently, we applied this approach in the experiments aimed at establishing trasncranial photoinhibition using eOPN3 (Fig. 4, N to P, and fig. S10, B to G). This procedure served as an important component of our experimental design, allowing us to reliably induce c-Fos expression in a high fraction of the OT population for subsequent investigations.

Transcranial photoinhibition of OT neurons in behaving pups

To investigate the impact of eOPN3-induced inhibition of OT neurons during MS on pups' behavior, AAV vectors encoding a Cre-dependent eOPN3-mScarlet transgene (rAAV2/1-hSyn1-SIO-eOPN3-mScarlet-WPRE; 7.3×10^{12} gc/ml; $n = 19$) or EGFP (rAAV2/1-hSyn1-DIO-EGFP; 7.3×10^{12} gc/ml; $n = 26$) were bilaterally injected into the PVN of OT-IRES-Cre P0 pups. At P12-P13 pups were implanted with an intact skull implant, and carefully monitored until the testing day. To minimize the incidence of aggressive behavior and infanticide by the dam towards the operated pups, dams were desensitized to the surgical substances starting 24 to 48 hours before the procedure (*89*). At P15-P16 pups underwent MS in a clear plexiglass cage (10 cm X 8 cm X 14 cm) and were subjected to 3-hour illumination using an Arduino-triggered red LED array (655 nm; 1 sec on, 1 sec off protocol; 191 μW/mm^2 at head level) positioned above the cage. During MS we installed a CM16/CMPA microphone (Avisoft) 20 cm above the cage surface, and sampled 5-min USV recordings at 20-min intervals, for a total of 8 recording sessions. Summary of USV count during MS, calculated as the mean number of USVs during the first and second halves of MS per mouse and averaged across mice. Four pups were not recorded during MS and excluded from the current analysis ($n_{(OT-EGFP)} = 24$; $n_{(OT-eOPN3)} = 17$). Then, following a brief recovery period (5 minutes; red light off), pups were removed to a new cage with an anesthetized dam to assess behavior upon reunion, as detailed in the "mother-pup assay."

To assess the impact of various features in the optogenetic experiment on pups' behavior during the reunion phase, we fit a general linear model (GLM) with the following features: (i) Mean fluorescence intensity (*FI*) of PVN sections for eOPN3- and EGFP-expressing pups. Values were averaged per mouse and standardized (Z-scores) per experimental group; (ii) MS USV attenuation index (*U*), computed using the following formula:

$$MSUSVindex = \frac{USV_{2nd} - USV_{1st}}{USV_{2nd} + USV_{1st}} \quad (8)$$

where USV_{1st} and USV_{2nd} are the averaged USV counts in MS first- and second-half recordings, respectively; (iii) Experimental group (*g*); (iv) Sex (*s*). The predicting features showed low multicollinearity with a variance inflation factor < 1.4 for all variables.

For the predicted variables of the model, we categorized pup behavior upon reunion into USV-related data ("vocal behavior"): (i) USV rate until first attachment; (ii) total USV count; (iii) USV rate outside attachment events; and non-USV-related data ("non-vocal behavior"): (i) total time attached; (ii) mean attachment length; (iii) time to first attachment; (iv) mean dam-pup distance; (v) entries to the dam's zone. One pup was excluded from the PCA due to incomplete anesthesia of the dam and missing data during the reunion phase ($n_{(OT-EGFP)} = 25$; $n_{(OT-eOPN3)} = 19$). We then standardized these variables and projected the Z-scored values onto the first two principal components (PCs) using principal component analysis (PCA), that were considered two independent responses of the GLM.

Finally, we used the features described above to predict PC1 and PC2 of pup behavior upon reunion. We removed pups where not all the predicting features could be measured (removing 7 pups where the mouse genotype was OT-Cre−/− and/or the mouse was not recorded during MS), as well as pups that were not recorded during reunion (removing 1 pup). This left $n = 37$ pups used for the model (EGFP: $n_{(F)} = 10$, $n_{(M)} = 10$; eOPN3: $n_{(F)} = 8$, $n_{(M)} = 9$). We used the *fitglm* function in MATLAB that received the following formula:

$$PCs = \beta_0 + \beta_1 \cdot FI + \beta_2 \cdot U + \beta_3 \cdot g + \beta_4 \cdot s + \beta_5 \cdot g \cdot s + \varepsilon \quad (9)$$

where *PCs* represents PC1 or PC2, β_0 is the intercept, β_1 through β_5 are the coefficients to be estimated for each predictor variable, and ε represents the error term. For the GLM models used in Fig. 5, F, G, I , and J, the normality assumption of residuals was tested by examining histograms and Kolmogorov-Smirnov test. For post-hoc Bonferroni-corrected comparisons of estimated marginal means we used the *emmeans* function in R to compare the experimental group and sex.

Blood sampling and quantification of plasma OT

Blood samples from the facial vein of P15 pups were collected in EDTA-coated tubes (MiniCollect, De-Grut) 1 hour after MS or from unseparated control pups. Blood samples were centrifuged at 1300*g* for 10 min at 4 °C, and 100 l plasma was collected for each mouse and stored at −80 °C until radioimmunoassay was performed [RIAgnosis, Munich, Germany; (*90*)]. Briefly, samples were preincubated for 60 min with 50 l rabbit anti-OT antibody, and then 10 l 125I-labeled tracer (Perkin Elmer, USA) was added to each aliquot. After an incubation period of 3 days at 4 °C, unbound radioactivity was precipitated by activated charcoal (Sigma Aldrich, USA). Under these conditions, an average of 50% of total counts are bound with <5% non-specific binding. The detection limit is in the 0.1 pg/sample range and the intra- and inter-assay variability is <10%.

Immunohistochemistry, imaging, and quantification

Mice were deeply anesthetized using pentobarbital (130 mg/kg; i.p.) and then transcardially perfused with ice-cold PBS (pH 7.4, 10 ml)

followed by 4% paraformaldehyde (PFA, 10 ml) solution. Heads were removed and post-fixed overnight at 4°C in 4% PFA. Then, brains were extracted and transferred to 30% sucrose solution for at least 24 hours. Coronal sections (30 m) were acquired using a microtome (Leica Microsystems) and preserved in a cryoprotectant solution (25% glycerol, 30% ethylene glycol in PBS, pH 6.7). Sections were washed 3×10 min in PBS, and incubated for 1 hour at room temperature (RT) in blocking solution: 20% normal horse serum (NHS), 0.5% triton-X100 in PBS. Primary antibodies were diluted in 2% NHS, 0.5% triton-X100 in PBS and incubated overnight at RT. The following antibodies were used: mouse anti-NP1 (OT staining; 1:2000; Merck; MABN844; RRID:AB_2315026), rabbit anti-cfos (1:500; Santa-Cruz; sc-52; RRID:AB_2106783), rabbit anti-cfos (1:2500; Cell Signaling; #2250; RRID:AB_2247211). The following day, the sections were washed 3×10 in PBS, then incubated for 2 h at RT with the following fluorophore-conjugated secondary antibodies: goat anti-rabbit Alexa 488 (1:300; Abcam; ab150077; RRID:AB_2630356), donkey anti-rabbit Cy5 (1:300; Jackson ImmunoResearch; 711-175-152; RRID:AB_2340607), goat anti-mouse Alexa 488 (1:300; ThermoFisher; A11029; RRID:AB_2534088), donkey anti-mouse Cy5 (1:300; Jackson ImmunoResearch; 715-175-151; RRID:AB_2340820), prepared in 2% NHS and PBS. Sections were washed 3×10 in PBS and stained with a nucleic acid dye (4,6-diamidino-2-phenylindole (DAPI), 1:10000). Finally, sections were mounted on gelatin-coated slides, dehydrated, and embedded in mounting medium (Aqua-Poly/Mount; Polysciences). Fluorescent images were acquired using a VS120 slide-scanning microscope (Olympus) at 10x or 20x magnification with DAPI, FITC and/or Cy3 and/or Cy5 channels.

The resulting images were then analyzed using ImageJ (2.14) to measure fluorescence within a specific region of interest (ROI). For unbiased ROI selection, in all experiments ROIs were identified using the DAPI channel and outlined based on anatomical landmarks in the Mouse Brain atlas (Paxinos and Franklin). The following analyses were done separately for each section, and individual values were averaged across sections of the target region per mouse, unless mentioned otherwise.

For images requiring c-Fos quantification (acquired with a 20x objective; 0.322^2 microns/pixel), we employed the pretrained StarDist 2D model for automatic segmentation of c-Fos+ nuclei [probability threshold = 0.5, nms = 0.3; (*91*)] and counted particles using the Analyzed Particles algorithm (size: 250-1500 pixels; circularity 0.7-1) in imageJ. c-Fos counts are normalized to the ROI's area (counts/mm^2).

To assess colocalization of c-Fos immunoreactivity with OT+/eOPN3+/EGFP+ ("Y") cells, we used StarDist segmentation previously applied for c-Fos analysis, and manually calculated the percentage of c-Fos+ Y+ cells out of the total number of Y+ cells within the ROI in both hemispheres. In addition, we divided the PVN into rostral (−0.58: −0.94 mm relative to bregma) and caudal (−1.06: −1.22 mm) sections and calculated the mean colocalization of c-Fos and OT immunoreactivity per PVN subarea. To assess the efficiency and specificity of eOPN3 viral expression in OT neurons, we counterstained PVN sections of eOPN3-expressing pups with an OT antibody and analyzed the data per hemisphere, assuming minimal crossover between hemispheres ($N = 8$ hemispheres; $n = 4$ mice). We then manually counted the fraction of mCherry+ cells out of OT+ cells, and the fraction of OT+ cells out of mCherry+ cells, respectively. For images requiring evaluation of eOPN3 or EGFP viral expression within the PVN, a fixed rectangle ROI was defined outlining the PVN bilaterally (excluding the 3rd ventricle). Mean fluorescence values were measured for Cy3 and FITC channels, respectively, to represent transgene expression in cells and projections within the ROI. One reunited pup ("Re") was excluded from the PVN analysis for technical reasons (related to Fig. 2). In all experiments, imaging acquisition parameters and the ensuing analysis pipeline were kept constant across mice, and experimenters were blinded to mouse experimental group during all steps that required manual annotations.

Identification of magnocellular and parvocellular OT neurons in P15 pups

As described previously in adult mice, P15 pups were transcardially perfused 8 days after two i.p. injections of FluoroGold (FG) over the course of 24 hours (1% in normal saline; 20 mg/kg; Santa Cruz; Sc-358883). Coronal sections of the PVN were stained with a primary antibody against FG (rabbit anti-FG; 1:100; RRID:AB_2314408), and FG immunoreactivity was visualized by an Alexa 488-conjugated secondary antibody (goat anti-rabbit; 1:800; Abcam; ab150077; RRID:AB_2630356). Expression patterns of FG and OT in the rostral-caudal axis of the PVN (-0.70:-1.22 mm relative to bregma) are shown in fig. S4A.

Statistical analyses

Details of specific statistical designs and appropriate tests are described for each analysis in the appropriate figure legend, Methods section, and throughout the text. Unless otherwise stated, data are summarized as the mean ± SEM, and single data points are marked on the appropriate figures, where n denotes the number of mice for behavioral trials and histological examinations, the number of USVs for cluster analysis and validation analysis of detection and classification tools, the number of nipple attachment events for PETH, and the number of cells for electrophysiological recordings. No statistical methods were used to predetermine sample sizes, but our sample sizes were chosen based on standards in the field. If applicable, animals were randomly assigned to experimental groups in in vivo studies. If applicable, data points excluded for any reason are detailed in the corresponding figure legend, and in the appropriate section in the Methods. Experimenters were blinded to the mouse experimental group, viral vector, drug and sex during experimental sessions and during initial analyses of behavioral and histological data. In Fig. 1 the experimenter was blind to the experimental groups only during data analysis. To control for nested effects, we used generalized LME models for statistical analysis and included mouse identity as a random intercept in our model Where applicable, we evaluated fixed and interaction effects in our models by using Type III ANOVA with Wald chi-square tests (*car* and *lme4* packages in R). All statistical tests presented in this manuscript are two-tailed. Significance was set at an alpha value of 0.05, and Bonferroni or FDR corrections were used when appropriate to correct for post hoc and multiple comparisons. Specific P values are detailed for each analysis in the corresponding figure legend, and in table S2, and significant comparisons are marked on the relevant figure panels. Levene's test was used to assess the equality of variances, and statistical parameters were adjusted accordingly when needed. When applicable, the data distribution was assumed to be normal, but this was not formally tested. All analyses and subsequent statistical tests were performed using MATLAB v.2018b (MathWorks), SPSS v.21 (IBM), R Statistical Software (R Project for Statistical Computing) and ImageJ (2.14).

REFERENCES AND NOTES

1. R. Menon, I. D. Neumann, Detection, processing and reinforcement of social cues: Regulation by the oxytocin system. *Nat. Rev. Neurosci.* **24**, 761–777 (2023). doi: 10.1038/s41583-023-00759-w; pmid: 37891399
2. H. Walum, L. J. Young, The neural mechanisms and circuitry of the pair bond. *Nat. Rev. Neurosci.* **19**, 643–654 (2018). doi: 10.1038/s41583-018-0072-6; pmid: 30301953
3. H. K. Choe *et al.*, Oxytocin mediates entrainment of sensory stimuli to social cues of opposing valence. *Neuron* **87**, 152–163 (2015). doi: 10.1016/j.neuron.2020.10.002; pmid: 33113347
4. G. Dölen, A. Darvishzadeh, K. W. Huang, R. C. Malenka, Social reward requires coordinated activity of nucleus accumbens oxytocin and serotonin. *Nature* **501** 179–184 (2013). doi: 10.1016/j.neuron.2020.10.002; pmid: 33113347
5. E. M. Lewis *et al.*, Parallel social information processing circuits are differentially impacted in autism. *Neuron* **108**, 659–675.e6 (2020). doi: 10.1016/j.neuron.2020.10.002; pmid: 33113347
6. M. Numan, T. R. Insel, *The Neurobiology of Parental Behavior*, vol. 1 (Springer Science & Business Media, 2006).
7. C. Dulac, L. A. O'Connell, Z. Wu, Neural control of maternal and paternal behaviors. *Science* **345**, 765–770 (2014). doi: 10.1126/science.1253291; pmid: 25124430

8. B. J. Marlin, M. Mitre, J. A. D'amour, M. V. Chao, R. C. Froemke, Oxytocin enables maternal behaviour by balancing cortical inhibition. *Nature* **520**, 499–504 (2015). doi: 10.1126/science.1253291; pmid: 25124430
9. T. R. Insel, L. J. Young, The neurobiology of attachment. *Nature Reviews Neuroscience* **2**, 129–136 (2001). doi: 10.1126/science.1253291; pmid: 25124430
10. S. Kojima, J. R. Alberts, Oxytocin mediates the acquisition of filial, odor-guided huddling for maternally associated odor in preweanling rats. *Hormones and Behavior* **60** 549–558 (2011). doi: 10.1126/science.1253291; pmid: 25124430
11. J. T. Winslow, T. R. Insel, The social deficits of the oxytocin knockout mouse. *Neuropeptides* **36**, 221–229 (2002) doi: 10.1126/science.1253291; pmid: 25124430
12. H. Hörnberg *et al.*, Rescue of oxytocin response and social behaviour in a mouse model of autism. *Nature* **584**, 252–256 (2020). doi: 10.1126/science.1253291; pmid: 25124430
13. O. Peñagarikano *et al.*, Exogenous and evoked oxytocin restores social behavior in the Cntnap2 mouse model of autism. *Science Translational Medicine* **7**, 271ra8 (2015) doi: 10.1126/science.1253291; pmid: 25124430
14. J. T. Winslow *et al.*, Infant vocalization, adult aggression, and fear behavior of an oxytocin null mutant mouse. *Hormones and Behavior* **37**, 145–155 (2000). doi: 10.1126/science.1253291; pmid: 25124430
15. Y. Takayanagi *et al.*, Pervasive social deficits, but normal parturition, in oxytocin receptor-deficient mice. *Proc. Natl. Acad. Sci. U.S.A.* **102**, 16096–16101 (2005) doi: 10.1126/science.1253291; pmid: 25124430
16. H. Harony-Nicolas *et al.*, Oxytocin improves behavioral and electrophysiological deficits in a novel Shank3-deficient rat. *eLife* **6**, e18904 (2017). doi: 10.7554/eLife.18904; pmid: 28139198
17. A. Meyer-Lindenberg, G. Domes, P. Kirsch, M. Heinrichs, Oxytocin and vasopressin in the human brain: social neuropeptides for translational medicine. *Nature Reviews* **12**, 524–538 (2011). doi: 10.1126/science.1253291; pmid: 25124430
18. L. J. Young, C. E. Barrett, Neuroscience. Can oxytocin treat autism? *Science* **347**, 825–826 (2015). doi: 10.1126/science.aaa8120; pmid: 25700501
19. T. R. Insel, The challenge of translation in social neuroscience: a review of oxytocin, vasopressin, and affiliative behavior. *Neuron* **65**, 768–779 (2010). doi: 10.1126/science.1253291; pmid: 25124430
20. L. Sikich *et al.*, Intranasal oxytocin in children and adolescents with autism spectrum disorder. *N. Engl. J. Med.* **385**, 1462–1473 (2021). doi: 10.1056/NEJMoa2103583; pmid: 34644471
21. A. J. Guastella *et al.*, The effect of oxytocin nasal spray on social interaction in young children with autism: A randomized clinical trial. *Mol. Psychiatry* **28**, 834–842 (2023). doi: 10.1038/s41380-022-01845-8; pmid: 36302965
22. K. J. Parker *et al.*, Intranasal oxytocin treatment for social deficits and biomarkers of response in children with autism. *Proc. Natl. Acad. Sci. U.S.A.* **114**, 8119–8124 (2017). doi: 10.1073/pnas.1705521114; pmid: 28696286
23. M. Opendak *et al.*, Bidirectional control of infant rat social behavior via dopaminergic innervation of the basolateral amygdala. *Neuron* **109**, 4018–4035.e7 (2021). doi: 10.1016/j.neuron.2021.09.041; pmid: 34706218
24. M. R. Zimmer, A. H. O. Fonseca, O. Iyilikci, R. D. Pra, M. O. Dietrich, Functional ontogeny of hypothalamic agrp neurons in neonatal mouse behaviors. *Cell* **178**, 44–59.e7 (2019). doi: 10.1016/j.cell.2019.04.026; pmid: 31104844
25. E. M. Blass, M. H. Teicher, Suckling. *Science* **210**, 15–22 (1980). doi: 10.1126/science.6997992; pmid: 6997992
26. J. Jansen, C. de Weerth, J. M. Riksen-Walraven, Breastfeeding and the mother–infant relationships–a review. *Dev. Rev.* **28**, 503–521 (2008). doi: 10.1016/j.dr.2008.07.001
27. C. P. Cramer, E. M. Blass, W. G. Hall, The ontogeny of nipple-shifting behavior in albino rats: Mechanisms of control and possible significance. *Dev. Psychobiol.* **13**, 165–180 (1980). doi: 10.1002/dev.420130208; pmid: 7188913
28. T. Toda, H. Kawasaki, The development of suckling behavior of neonatal mice is regulated by birth. *Mol. Brain* **7**, 8 (2014). doi: 10.1186/1756-6606-7-8; pmid: 24507718
29. D. T. Sangiamo, M. R. Warren, J. P. Neunuebel, Ultrasonic signals associated with different types of social behavior of mice. *Nat. Neurosci.* **23**, 411–422 (2020). doi: 10.1038/s41593-020-0584-z; pmid: 32066980
30. A. H. Fonseca, G. M. Santana, G. M. Bosque Ortiz, S. Bampi, M. O. Dietrich, Analysis of ultrasonic vocalizations from mice using computer vision and machine learning. *eLife* **10**, e59161 (2021). doi: 10.7554/eLife.59161; pmid: 33787490
31. J. M. S. Grimsley, J. J. M. Monaghan, J. J. Wenstrup, Development of social vocalizations in mice. *PLOS ONE* **6**, e17460 (2011). doi: 10.1371/journal.pone.0017460; pmid: 21408007
32. I. Merchenthaler, Neurons with access to the general circulation in the central nervous system of the rat: A retrograde tracing study with fluoro-gold. *Neuroscience* **44**, 655–662 (1991). doi: 10.1016/0306-4522(91)90085-3; pmid: 1721686
33. Y. Zhang *et al.*, Fast and sensitive GCaMP calcium indicators for imaging neural populations. *Nature* **615**, 884–891 (2023). doi: 10.1038/s41586-023-05828-9; pmid: 36922596
34. T.-L. Sterley *et al.*, Social transmission and buffering of synaptic changes after stress. *Nat. Neurosci.* **21**, 393–403 (2018). doi: 10.1038/s41593-017-0044-6; pmid: 29311741
35. J. A. Luther, J. G. Tasker, Voltage-gated currents distinguish parvocellular from magnocellular neurones in the rat hypothalamic paraventricular nucleus. *J. Physiol.* **523**, 193–209 (2000). doi: 10.1111/j.1469-7793.2000.t01-1-00193.x
36. Materials and methods are available as supplementary materials.
37. J. Chen *et al.*, Flexible scaling and persistence of social vocal communication. *Nature* **593**, 108–113 (2021). doi: 10.1038/s41586-021-03403-8; pmid: 33790464
38. B. Knutson, J. Burgdorf, J. Panksepp, Ultrasonic vocalizations as indices of affective states in rats. *Psychol. Bull.* **128**, 961–977 (2002). doi: 10.1037/0033-2909.128.6.961
39. J. Panksepp, Beyond a Joke: From Animal Laughter to Human Joy? Playing Nature's Game. *Science* **308**, 62–63 (2005). doi: 10.1126/science.1112066; pmid: 15802592
40. M. Mahn *et al.*, Efficient optogenetic silencing of neurotransmitter release with a mosquito rhodopsin. *Neuron* **109**, 1621–1635.e8 (2021). doi: 10.1016/j.neuron.2021.03.013; pmid: 33979634
41. G. E. Hoffman, M. S. Smith, J. G. Verbalis, c-Fos and related immediate early gene products as markers of activity in neuroendocrine systems. *Front. Neuroendocrinol.* **14**, 173–213 (1993). doi: 10.1006/frne.1993.1006; pmid: 8349003
42. M. T. Hasan *et al.*, A fear memory engram and its plasticity in the hypothalamic oxytocin system. *Neuron* **103**, 133–146.e8 (2019). doi: 10.1016/j.neuron.2019.04.029; pmid: 31104950
43. V. Grinevich, R. Stoop, Interplay between Oxytocin and Sensory Systems in the Orchestration of Socio-Emotional Behaviors. *Neuron* **99**, 887–904 (2018). doi: 10.1016/j.neuron.2018.07.016
44. R. C. Froemke, L. J. Young, Oxytocin, neural plasticity, and social behavior. *Annu. Rev. Neurosci.* **44**, 359–381 (2021). doi: 10.1146/annurev-neuro-102320-102847
45. R. W. Elwood, F. Keeling, Temporal organization of ultrasonic vocalizations in infant mice. *Dev. Psychobiol.* **15**, 221–227 (1982). doi: 10.1002/dev.420150306
46. J. L. Silverman, M. Yang, C. Lord, J. N. Crawley, Behavioural phenotyping assays for mouse models of autism. *Nat. Rev. Neurosci.* **11**, 490–502 (2010). doi: 10.1038/nrn2851
47. C. V. Portfors, Types and functions of ultrasonic vocalizations in laboratory rats and mice. *J. Am. Assoc. Lab. Anim. Sci.* **46**, 28–34 (2007). pmid: 17203913
48. G. A. Matthews, K. M. Tye, Neural mechanisms of social homeostasis. *Ann. N. Y. Acad. Sci.* **1457**, 5–25 (2019). doi: 10.1111/nyas.14016
49. Y. Li *et al.*, Neurons for infant social behaviors in the mouse zona incerta. *Science* **385**, 409–416 (2024). doi: 10.1126/science.adk7411; pmid: 39052814
50. X. Zhao *et al.*, Sex- and context-dependent effects of acute isolation on vocal and non-vocal social behaviors in mice. *PLOS ONE* **16**, e0255640 (2021). doi: 10.1371/journal.pone.0255640; pmid: 34469457
51. X. Zhao *et al*., Short-term social isolation acts on hypothalamic neurons to promote social behavior in a sex-and context-dependent manner. bioRxiv 2023.11.20.567901v3 [Preprint] (2023); https://www.biorxiv.org/content/10.1101/2023.11.20.567901v3.full.pdf.
52. D. Liu *et al.*, A hypothalamic circuit underlying the dynamic control of social homeostasis. *Nature* **640**, 1000–1010 (2025). doi: 10.1038/s41586-025-08617-8; pmid: 40011768
53. P. Jensen, B. Algers, An ethogram of piglet vocalizations during suckling. *Appl. Anim. Ethol.* **11**, 237–248 (1984). doi: 10.1016/0304-3762(84)90030-0
54. B. Algers, P. Jensen, Communication during suckling in the domestic pig. Effects of continuous noise. *Appl. Anim. Behav. Sci.* **14**, 49–61 (1985). doi: 10.1016/0168-1591(85)90037-1
55. J. Boulanger-Bertolus, M. Rincón-Cortés, R. M. Sullivan, A.-M. Mouly, Understanding pup affective state through ethologically significant ultrasonic vocalization frequency. *Sci. Rep.* **7**, 13483 (2017). doi: 10.1038/s41598-017-13518-6; pmid: 29044126
56. M. A. Hofer, Multiple regulators of ultrasonic vocalization in the infant rat. *Psychoneuroendocrinology* **21**, 203–217 (1996). doi: 10.1016/0306-4530(95)00042-9; pmid: 8774063
57. A. H. Veenema, Toward understanding how early life social experiences alter oxytocin- and vasopressin-regulated social behaviors. *Horm. Behav.* **61**, 304–312 (2012). doi: 10.1016/j.yhbeh.2011.12.002
58. A. M. Kelly, L. C. Hiura, A. G. Ophir, Rapid nonapeptide synthesis during a critical period of development in the prairie vole: Plasticity of the paraventricular nucleus of the hypothalamus. *Brain Struct. Funct.* **223**, 2547–2560 (2018). doi: 10.1007/s00429-018-1640-2
59. S. Musardo, A. Contestabile, M. Knoop, O. Baud, C. Bellone, Oxytocin neurons mediate the effect of social isolation via the VTA circuits. *eLife* **11**, (2022). doi: 10.7554/eLife.73421
60. Y. Tang *et al.*, Social touch promotes interfemale communication via activation of parvocellular oxytocin neurons. *Nat. Neurosci.* **23**, 1125–1137 (2020). doi: 10.1038/s41593-020-0674-y; pmid: 32719563
61. M. Eliava *et al.*, A new population of parvocellular oxytocin neurons controlling magnocellular neuron activity and inflammatory pain processing. *Neuron* **89**, 1291–1304 (2016). doi: 10.1016/j.neuron.2016.01.041
62. M. Iwasaki *et al.*, An analgesic pathway from parvocellular oxytocin neurons to the periaqueductal gray in rats. *Nat. Commun.* **14**, 1066 (2023). doi: 10.1038/s41467-023-36641-7; pmid: 36828816
63. D. Atasoy, J. N. Betley, H. H. Su, S. M. Sternson, Deconstruction of a neural circuit for hunger. *Nature* **488**, 172–177 (2012). doi: 10.1038/nature11270

64. Y. Liu *et al.*, Molecular and cellular mechanisms of the first social relationship: A conserved role of 5-HT from mice to monkeys, upstream of oxytocin. *Neuron* **111**, 1468–1485.e7 (2023). doi: 10.1016/j.neuron.2023.02.010; pmid: 36868221
65. V. Grinevich, M. G. DesarmÃ©nien, B. Chini, M. Tauber, F. Muscatelli, Ontogenesis of oxytocin pathways in the mammalian brain: Late maturation and psychosocial disorders. *Front. Neuroanat.* **8**, 164 (2014). doi: 10.3389/fnana.2014.00164
66. B. Jurek, I. D. Neumann, The oxytocin receptor: From intracellular signaling to behavior. *Physiol. Rev.* **98**, 1805–1908 (2018). doi: 10.1152/physrev.00031.2017
67. E. A. D. Hammock, Developmental perspectives on oxytocin and vasopressin. *Neuropsychopharmacology* **40**, 24–42 (2015). doi: 10.1038/npp.2014.120
68. K. L. Thompson *et al.*, Pharmacokinetics and disposition of the oxytocin receptor antagonist L-368,899 in rats and dogs. *Drug Metab. Dispos.* **25**, 1113–1118 (1997). pmid: 9321512
69. V. N. Barros *et al.*, The pattern of c-Fos expression and its refractory period in the brain of rats and monkeys. *Front. Cell. Neurosci.* **9**, 72 (2015). doi: 10.3389/fncel.2015.00072; pmid: 25814929
70. J. I. Morgan, D. R. Cohen, J. L. Hempstead, T. Curran, Mapping patterns of c-fos expression in the central nervous system after seizure. *Science* **237**, 192–197 (1987). doi: 10.1126/science.3037702; pmid: 3037702
71. M. Anisimova *et al.*, Neuronal FOS reports synchronized activity of presynaptic neurons. BioRxiv 2023.09.04.556168v1 [Preprint] (2023); https://doi.org/10.1101/2023.09.04.556168.
72. H. K. Caldwell, Oxytocin and sex differences in behavior. *Curr. Opin. Behav. Sci.* **23**, 13–20 (2018). doi: 10.1016/j.cobeha.2018.02.002
73. E. Ey *et al.*, Shank2 mutant mice display hyperactivity insensitive to methylphenidate and reduced flexibility in social motivation, but normal social recognition. *Front. Mol. Neurosci.* **11**, 365 (2018). doi: 10.3389/fnmol.2018.00365
74. D. K. Oller *et al.*, Sex differences in infant vocalization and the origin of language. *iScience* **26**, 106884 (2023). doi: 10.1016/j.isci.2023.106884; pmid: 37378320
75. K. M. Dumais, A. H. Veenema, Vasopressin and oxytocin receptor systems in the brain: Sex differences and sex-specific regulation of social behavior. *Front. Neuroendocrinol.* **40**, 1–23 (2016). doi: 10.1016/j.yfrne.2015.04.003; pmid: 25951955
76. M. Maroun, A. Sarussi-Elyahu, A. Yaseen, O. A. Hatoum, M. Kritman, Sex-dimorphic role of prefrontal oxytocin receptors in social-induced facilitation of extinction in juvenile rats. *Transl. Psychiatry* **10**, 356 (2020). doi: 10.1038/s41398-020-01040-9; pmid: 33077706

ACKNOWLEDGMENTS

We thank all Yizhar Lab members for fruitful discussions; S. Devore, Y. Ziv, and G. Ginosar for comments on the manuscript; A. Benjamin and G. Avineri for advice on modeling; Y. Cohen for advice on acoustic recording and analysis; Y. Sarusi, R. B. T. Perry, I. Ulitsky, and R. Eilam-Altstadter for advice on histology; Y. Kuperman for assistance with sample collection; D. Goldian for assistance with electronics; A. Jahanfard for assistance with scientific instrumentation. O. Rozenberg, E. Tamar, and E. Madmon for support with animal husbandry and care; and Y.S.Z. for her endless support. [Figures 1 to 5 and S4, S8, and S18 were created with BioRender.com.] **Funding:** This work was supported by grants from the National Institutes of Health (1U01NS128537-01 to OY), the European Horizon 2020 Program (ERC CoG PrefrontalMap 819496; RIA DEEPER 101016787 O.Y.) and the Israel Science Foundation (ISF 3131/20 to O.Y.). O.Y. is the incumbent of the Joseph and Wolf Lebovic Charitable Foundation Chair for Research in Neuroscience. The Yizhar lab is further supported by the Laura and Anthony Beck and Family Fund for Research in Neuroscience Related to Youth at Risk, and by the Paul and Lucie Schwartz - Georges and Vera Gersen Laboratory. **Author contributions:** Conceptualization: D.D.Z. and O.Y.; Methodology: D.D.Z., M.K. and O.Y.; Investigation: D.D.Z., R.B., J.D., J.W., A.L., S.A., S.C. and A.A.; Data Curation: D.D.Z., R.B., J.D. and J.W.; Formal Analysis: D.D.Z. and R.B.; Software: D.D.Z. and I.P.; Visualization: D.D.Z., R.B. and J.W.; Writing – Original Draft: D.D.Z. and O.Y.; Writing – Review & Editing: D.D.Z., R.B. and O.Y.; Supervision: O.Y.; Project Administration: D.D.Z. and O.Y.; Funding Acquisition: O.Y.; Resources: O.Y. **Competing interests:** O.Y. is listed as an inventor on a patent application ("Bistable type ii opsins and uses thereof", US20210403518A1) filed with the US Patent Office regarding eOPN3 and serves as a consultant for Modulight.bio. The other authors declare no competing interests. **Data and materials availability:** The data presented in this manuscript are freely available at (*92*). Custom code used for data analysis is available from the authors upon request.

SUPPLEMENTARY MATERIALS

science.org/doi/10.1126/science.ado5609
Figs. S1 to S14; Tables S1 and S2; References (*77*–*92*); Movies S1 and S2

Submitted 8 February 2024; resubmitted 20 March 2025; accepted 21 July 2025
10.1126/science.ado5609